Economic Geology, v. 116, no. 3, pp. 581–606

Evolution of Multistage Hydrothermal Fluids in the Luoboling Porphyry Cu-Mo Deposit, Zijinshan Ore Field, Fujian Province, China: Insights from LA-ICP-MS Analyses of Fluid Inclusions

Xiao-Yu Zhao,[1,2] Hong Zhong,[1,2,†] Rui-Zhong Hu,[1,2] Wei Mao,[1] Zhong-Jie Bai,[1] Ting-Guang Lan,[1] and Kai Xue[3]

[1]*State Key Laboratory of Ore Deposit Geochemistry, Institute of Geochemistry, Chinese Academy of Sciences, Guiyang 550081, China*

[2]*University of Chinese Academy of Sciences, Beijing 100049, China*

[3]*Zijin Mining Group Co. Ltd., Shanghang 364200, China*

Abstract

The Luoboling Cu-Mo deposit, with 1.4 million tons (Mt) Cu and 0.11 Mt Mo, is the largest porphyry deposit in the Zijinshan district of southeast China. Mineralization at Luoboling is divided into premineralization, syn-mineralization, and late-mineralization stages. Consistent Cs/(Na + K) ratios in fluid inclusions suggest that the mineralizing fluids originated from a common source—the Luoboling granodiorite porphyry. The absence of initial supercritical fluid inclusions and abundant coexisting vapor and brine fluid inclusions imply that the fluids exsolved at low-pressure two-phase conditions, with temperatures of 250° to 600°C and salinities of 30 to 60 wt % NaCl equiv (brines) and <10 wt % NaCl equiv (vapors). The deposit formed at ~120 to 800 bar, corresponding to the depths of ~1.2 to 3.2 km (assuming a transition from lithostatic to hydrostatic load). Metals such as Mo (up to 77 ppm), Pb (up to 8,800 ppm), Zn (up to 13,000 ppm), and Ag (up to 130 ppm) migrated mainly in brines. Although vapor inclusions have high concentrations of Cu (up to 20,000 ppm), hypersaline fluid was the major medium for Cu transport and precipitation. The successive precipitation of Mo and Cu occurred when fluids cooled to ~500°C and ~350° to 450°C, respectively. The late-stage quartz-pyrite veins with phyllic alteration were formed by Cu-rich magmatic hydrothermal fluids. The Zijinshan epithermal Cu-Au deposit and the Luoboling porphyry Cu-Mo deposit originated from independent hydrothermal systems. Nonetheless, the increasing trends of Pb, Zn, and Ag concentrations in different stage inclusions from Luoboling imply potential for distal Pb-Zn-Ag mineralization.

Introduction

The Zijinshan ore district, located in Fujian Province, is the largest epithermal mining district in China (Mao et al., 2007), with metal reserves of more than 399 tons (t) Au, 4.1 Mt Cu, 6,339 t Ag, and 0.11 Mt Mo (Zhang, 2013). This district hosts different types of deposits, including the Luoboling porphyry Cu-Mo deposit, Zijinshan high-sulfidation epithermal Cu-Au deposit, Yueyang intermediate-sulfidation Ag polymetallic epithermal deposit, and Wuziqilong hybrid high-sulfidation porphyry Cu deposit (e.g., Zhang et al., 2001, 2003, 2005; Jiang et al., 2013; Duan et al., 2017; Xu et al., 2017).

Numerous studies have been conducted on the Zijinshan high-sulfidation epithermal Cu-Au deposit, as it hosts the largest Au and Cu reserves within the ore field (e.g., Zhang et al., 1991, 2003, 2005; Chen, 1996; So et al., 1998; Liu et al., 2016, 2017; Jiang et al., 2017; Li and Jiang, 2017; Piquer et al., 2017; Wu et al., 2017, 2018; Huang et al., 2018; Zhong et al., 2018; Chen et al., 2019). Luoboling is the largest porphyry deposit in this district, with metal reserves of 1.4 Mt Cu and 0.11 Mt Mo (Zhang, 2013). Zhong et al. (2014) discussed physical and chemical evolution of ore-forming fluids at Luoboling through microthermometry of fluid inclusions and H-O isotopes but did not conduct major and trace element analyses of fluid inclusions.

In this paper, based on detailed geologic observations, scanning electron microscope cathodoluminescence (SEM-CL) was used to refine the mineralization stages at Luoboling. Petrographic and microthermometric analyses of fluid inclusions were conducted, and laser ablation-inductively coupled plasma-mass spectrometry (LA-ICP-MS) was used to quantitatively determine the compositions of individual fluid inclusions. These data are used to constrain the physical, chemical, and compositional evolution of ore-forming fluids, transport processes, and precipitation mechanisms of Mo and Cu and to assess whether there is a genetic relationship between the Luoboling porphyry and Zijinshan high-sulfidation epithermal deposit, which is significant for regional exploration.

Regional Geology

The South China block comprises the northwestern Yangtze block and the southeastern Cathaysia block (Fig. 1a). Sinian, early Paleozoic, late Paleozoic, and Mesozoic strata and Caledonian to Yanshanian magmatic rocks are exposed in the area (Fig. 1b). Extensive Yanshanian magmatism occurred in the Cathaysia block, southeastern coastal area of China, because of subduction of the Paleo-Pacific Plate (Mao et al., 2013). Widespread Cretaceous magmatism produced numerous Pb-Zn-Ag, Cu-Au, and W-Sn deposits in the Zhejiang, Fujian, and Guangdong provinces (Mao et al., 2013). The regional structural framework during mineralization was controlled by NE-trending faults, such as the Zhenghe-Dapu and Nanping-Ninghua faults, and NW-trending faults, such as the Shanghang-Yunxiao and Yongan-Quanzhou faults (Fig. 1b).

The Zijinshan Cu-Au-Mo-Ag ore field is located in southwestern Fujian Province in the central area of the Cathaysia block and at the intersection of the Xuanhe anticlinorium and

[†]Corresponding author: e-mail, zhonghong@vip.gyig.ac.cn

ISSN 0361-0128; doi:10.5382/econgeo.4788; 26 p.
Digital appendices are available in the online Supplements section.

Submitted: September 5, 2019 / Accepted: August 4, 2020

the Shanghang-Yunxiao fault (Fig. 1a, b; Zhang et al., 2003, 2005; Wang et al., 2009; Qiu et al., 2010; Jiang et al., 2017; Wu et al., 2017, 2018). Several deposits and prospects have been discovered within the Zijinshan ore field, including porphyry (Luoboling, Xinan, and Jintonghu Cu-Mo; Xue and Ruan, 2008; Zhong et al., 2011, 2014; Liang et al., 2012; Huang et al., 2013; Wu et al., 2013; Li et al., 2016), high-sulfidation epithermal (Zijinshan and Dajigang Cu-Au, Ermiaogou Cu; So et al., 1998; Zhang et al., 2003, 2005; Li et al., 2013; Chen et al., 2019), hybrid porphyry-high sulfidation (Wuziqilong and Longjiangting Cu; Chen et al., 2011, 2015), and intermediate-sulfidation epithermal deposits (Yueyang Ag-Au-Cu; Zhong et al., 2017; Fig. 1c). Northeast- and NW-trending faults controlled the distribution of intrusions and mineralization and cut or reformed Neoproterozoic to Cretaceous strata in the ore field (Fig. 1c; Piquer et al., 2017).

Different lithostratigraphic units are distributed around central intrusive rocks in the district (Fig. 1c). These units include the Neoproterozoic Louziba Group, late Paleozoic clastic sedimentary rocks, Early Cretaceous volcanic assemblages, and Quaternary alluvial sediments (Fig. 1c). The Louziba Group is mainly composed of low-grade metamorphosed shallow marine sedimentary rocks, including two-mica schist, muscovite schist, phyllite, metasiltstone, and metasandstone (Zhong et al., 2011, 2014, 2017). Minor siliceous rocks occur at the top of strata (Chen et al., 2019). Late Paleozoic sedimentary rocks constitute the Late Devonian Tianwadong and Taozikeng Formations and the early Carboniferous Lindi Formation (Zhong et al., 2014). The Tianwadong Formation mainly contains upper siltstone and lower quartz conglomerate, whereas the Taozikeng Formation is composed of siltstone and gravel sandstone (Chen et al., 2019). Besides siltstone and gravel sandstone, limestone also occurs in the Lindi Formation (Chen et al., 2019). The Early Cretaceous Shimaoshan Group, comprising dacite, rhyolite, ignimbrite, and tuff, as well as minor conglomerate intercalations, is distributed widely in the southeastern part of the ore field (Fig. 1c; Zhong et al., 2011, 2014, 2017). These rocks unconformably overlie the Louziba Group and the Zijinshan granite batholith (Fig. 1c; Zhong et al., 2014).

Intrusive rocks in the Zijinshan district include the Middle Jurassic Zijinshan granite batholith, Late Jurassic Caixi monzogranite pluton, Early Cretaceous Sifang granodiorite, Luoboling granodiorite porphyry, and Zhongliao granodiorite (Fig. 1c). The Zijinshan granite batholith is composed of three subunits, including the southern Jingmei medium- to coarse-grained porphyritic granite, middle Wulongsi medium- to fine-grained granite, and northern Jinglongqiao fine-grained granite plutons. They were emplaced in the early Yanshanian between 168 ± 4 and 149 ± 2 Ma (Zhou and Chen, 1996; Zhang et al., 2001; Zhao et al., 2008; Jiang et al., 2013; Yu et al., 2013). The small-scale Caixi pluton is only exposed in the eastern part of the district and has zircon U-Pb ages of 150 ± 2 to 146.4 ± 8.6 Ma (Zhao et al., 2008; Hu et al., 2012; Yu et al., 2013). The Sifang pluton is distributed in the northeast of the district and was emplaced into the Wulongsi pluton around 112 ± 1 to 104.8 ± 1.7 Ma (Hu et al., 2012; Jiang et al., 2013; Yu et al., 2013). The Luoboling pluton is related to porphyry mineralization at Luoboling and was intruded by the Zhongliao pluton. Both the Luoboling and Zhongliao plutons are exposed over an area of ~0.5 km^2 in the eastern ore field and intruded into the Sifang pluton around 107 ± 1.6 to 103.1 ± 1.1 Ma and 99.5 ± 1.6 to 95.9 ± 0.6 Ma, respectively (Figs. 1c, 2a; Huang et al., 2013, 2018; Yu et al., 2013; Li and Jiang, 2015; Li et al., 2016; Duan et al., 2017). Small-scale Cretaceous polymict lithic breccia pipes and dacitic tuffs and porphyries associated with Cu-Au mineralization crop out locally in the ore field (Fig. 1c), with zircon U-Pb ages from 112.9 ± 1.2 to 96 ± 2 Ma (Hu et al., 2012; Jiang et al., 2013; Li et al., 2013; Yu et al., 2013; Duan et al., 2017; Huang et al., 2018; Pan et al., 2019).

Deposit Geology

The Luoboling porphyry Cu-Mo deposit contains 1.4 Mt of Cu at an average grade of 0.3% and 0.11 Mt of Mo at an average grade of 0.036% (Zhang, 2013). It is located in the northeastern part of the Zijinshan ore field (Fig. 1c), ~2 km northeast of the Zijinshan high-sulfidation Cu-Au deposit. The Cu-Mo orebodies of Luoboling exhibit a close spatial relationship with the Sifang granodiorite, Luoboling granodiorite porphyry, and Zhongliao porphyritic biotite granodiorite (Fig. 2b-e). The Luoboling pluton is the major host to Cu-Mo mineralization and is also commonly interpreted to be the mineralization source (Zhong et al., 2014). Minor biotite granodiorite porphyry dikes locally intrude the Luoboling granodiorite pluton and yield a younger zircon U-Pb age of 97.6 ± 2.1 Ma (Huang et al., 2013). However, Pan et al. (2019) recently reported a zircon U-Pb age of 133.6 ± 1.1 Ma for these rocks, which is too old to be consistent with geologic observation and is possibly attributed to the interference of inherited zircons. The Sifang pluton hosts minor mineralization in the upper part of the deposit (Fig. 2). The barren and fresh Zhongliao pluton intruded the Luoboling pluton and cut Cu-Mo orebodies at depth, and drilling stops whenever this pluton is intersected (Fig. 2). The youngest intrusion is a NW-trending quartz syenite porphyry dike that cuts the other intrusions and Cu-Mo orebodies (Fig. 2d, e).

The Cu-Mo orebodies at Luoboling are located on the northeastern side of the Luoboling pluton (Fig. 2). These orebodies have dimensions of ~1,200 m long and ~800 m laterally and extend ~900 m vertically from ~–400- to 500-m elevation (Fig. 2b-e). The orebodies vary between 50 and 500 m thick and have shapes that are saddle-like, arcuate, or lenticular (Fig. 2b-e; Zhong et al., 2014). High-grade ores are mainly concentrated in the upper parts of the deposit (Fig. 2). Molybdenite Re-Os dating results indicate that the deposit formed at 105.5 ± 2.2 to 104.6 ± 1.0 Ma (Liang et al., 2012; Zhong et al., 2014; Duan et al., 2017; Li and Jiang, 2017).

Fig. 1. (a) Simplified geologic map of eastern South China (modified after Li and Jiang, 2017). (b) Regional geologic map of Fujian Province (modified after Wu et al., 2017). (c) Geologic map of the Zijinshan ore field showing distributions of magmatic and sedimentary rocks, ore deposits, and faults (modified after Zijin Mining Group Co., unpub. data, 2018, and Pan et al., 2019). Abbreviations: Fm = formation, Gp = group.

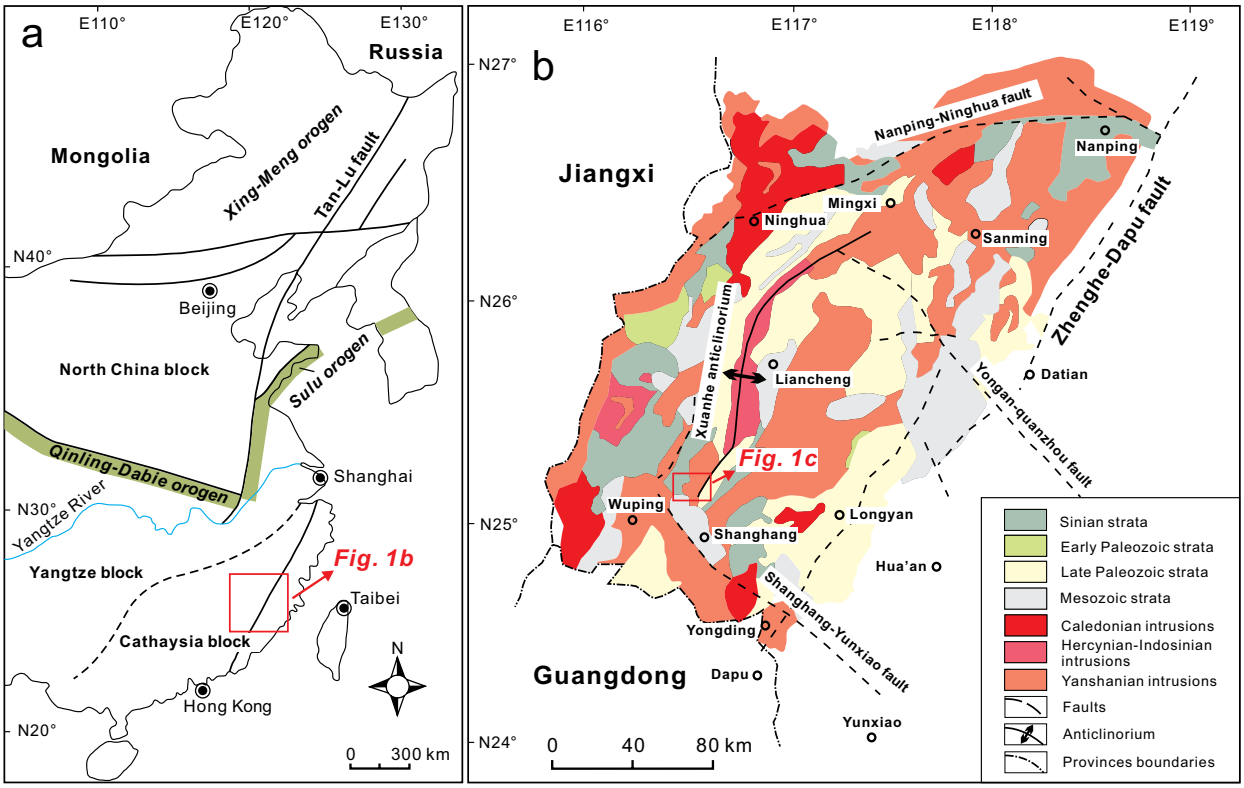

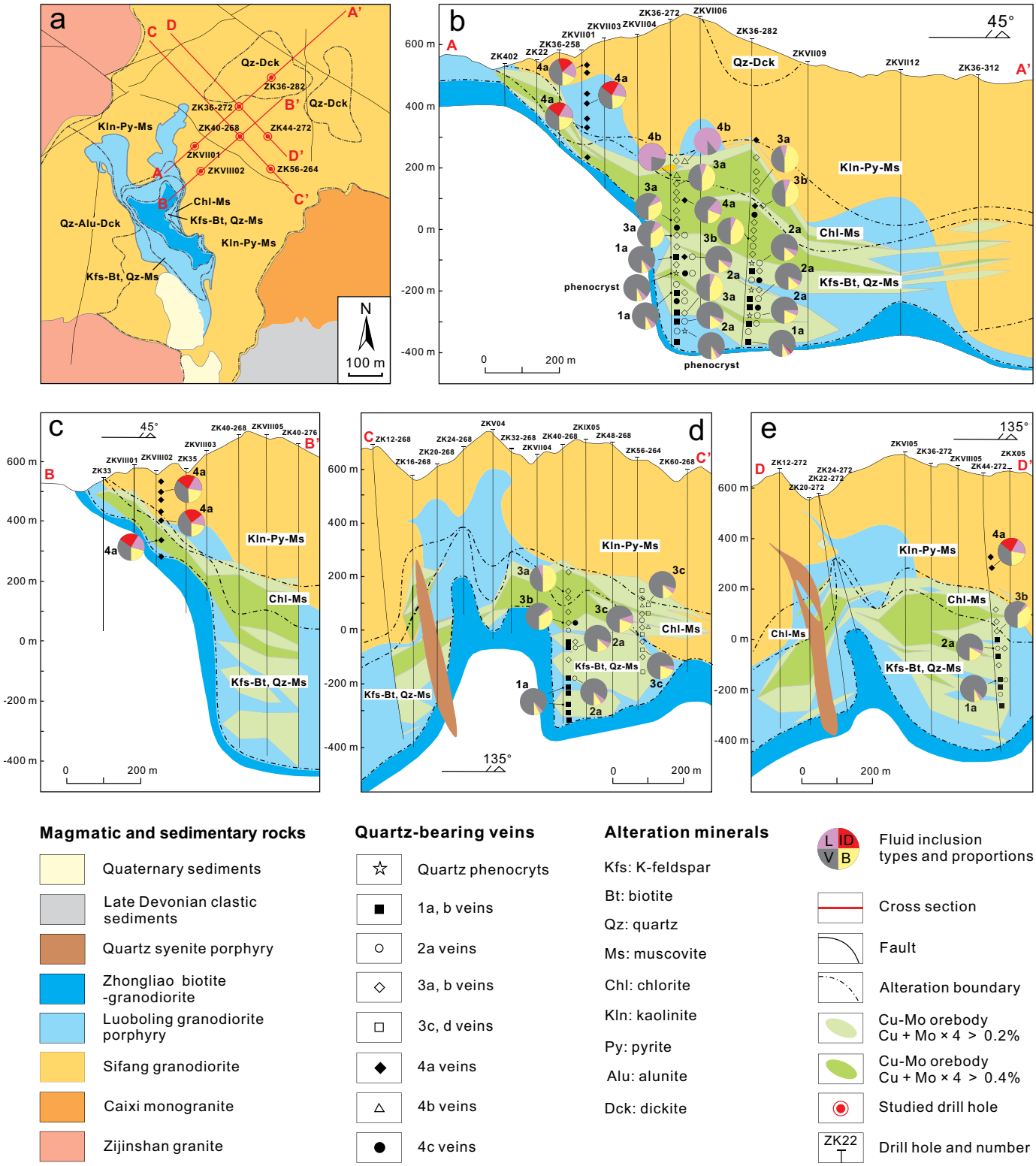

Magmatic and sedimentary rocks

- Quaternary sediments
- Late Devonian clastic sediments
- Quartz syenite porphyry
- Zhongliao biotite -granodiorite
- Luoboling granodiorite porphyry
- Sifang granodiorite
- Caixi monogranite
- Zijinshan granite

Quartz-bearing veins

- Quartz phenocryts
- 1a, b veins
- 2a veins
- 3a, b veins
- 3c, d veins
- 4a veins
- 4b veins
- 4c veins

Alteration minerals

Kfs: K-feldspar
Bt: biotite
Qz: quartz
Ms: muscovite
Chl: chlorite
Kln: kaolinite
Py: pyrite
Alu: alunite
Dck: dickite

- Fluid inclusion types and proportions (L, ID, V, B)
- Cross section
- Fault
- Alteration boundary
- Cu-Mo orebody Cu + Mo × 4 > 0.2%
- Cu-Mo orebody Cu + Mo × 4 > 0.4%
- Studied drill hole
- ZK22 Drill hole and number

Fig. 2. (a) Geologic map of Luoboling showing the surface lithologies, structures, and hydrothermal alteration domains. (b) Geologic profile of No. 36 exploration line showing lithology, mineralization, and alteration. (c) Geologic profile of No. 40 exploration line. (d) Geologic profile of No. 268 exploration line. (e) Geologic profile of No. 272 exploration line. Modified after unpublished data from the Zijin Mining Group Co. The spatial distributions of veins and associated fluid inclusion types are illustrated in the drill holes. Fluid inclusion abbreviations: B = brine inclusion, ID = intermediate-density inclusion, L = liquid-rich inclusion, V = vapor-rich inclusion.

Hydrothermal alteration affected the Luoboling and Sifang plutons widely, producing a zoned pattern of K-feldspar-biotite, quartz-muscovite, chlorite-muscovite, and kaolinite-muscovite-pyrite alteration zones from bottom to top (Figs. 2, 3, 4; Table 1). The deep K-feldspar-biotite alteration zone has been overprinted by quartz-muscovite alteration, particularly between ~–200 and 50 m above sea leavel (a.s.l.) (Fig. 2). This overprinting is obvious in the central and northern parts of the deposit but is not common in the southwestern and southern drill holes (Fig. 2). Secondary K-feldspar has been partly or completely replaced by fine-grained muscovite and quartz (Fig. 3e). Quartz-dickite alteration affected the northeastern part of the deposit (Fig. 2a), whereas extensive quartz-dickite-alunite alteration formed to the west (Fig. 2a). Molybdenum mineralization at Luoboling is generally associated with K-feldspar-biotite alteration in the lower parts of the deposit, whereas Cu mineralization is mainly associated with quartz-muscovite and chlorite-muscovite alteration in the middle to upper parts of the deposit (Fig. 2).

Sulfides and oxides at Luoboling include chalcopyrite, molybdenite, pyrite, galena, bornite, magnetite, and hematite (Fig. 4). Minor digenite and covellite were reported in previous publications (Zhong et al., 2014; Li and Jiang, 2017) but have not been observed in this study.

Mineralization at Luoboling produced stockwork veins (Fig. 5) and minor disseminated ores. Based on crosscutting relationships, mineral assemblages, and related alteration of hydrothermal veins, four paragenetic stages have been determined: premineralization stage 1, Mo mineralization stage 2, Cu-Mo mineralization stage 3, and late-mineralization stage 4. A total of 12 vein types have been recognized from Luoboling (Fig. 5; Table 2).

The premineralization stage (stage 1) comprises sulfide-barren quartz veins (Fig. 5a-f; Table 2), which mainly developed

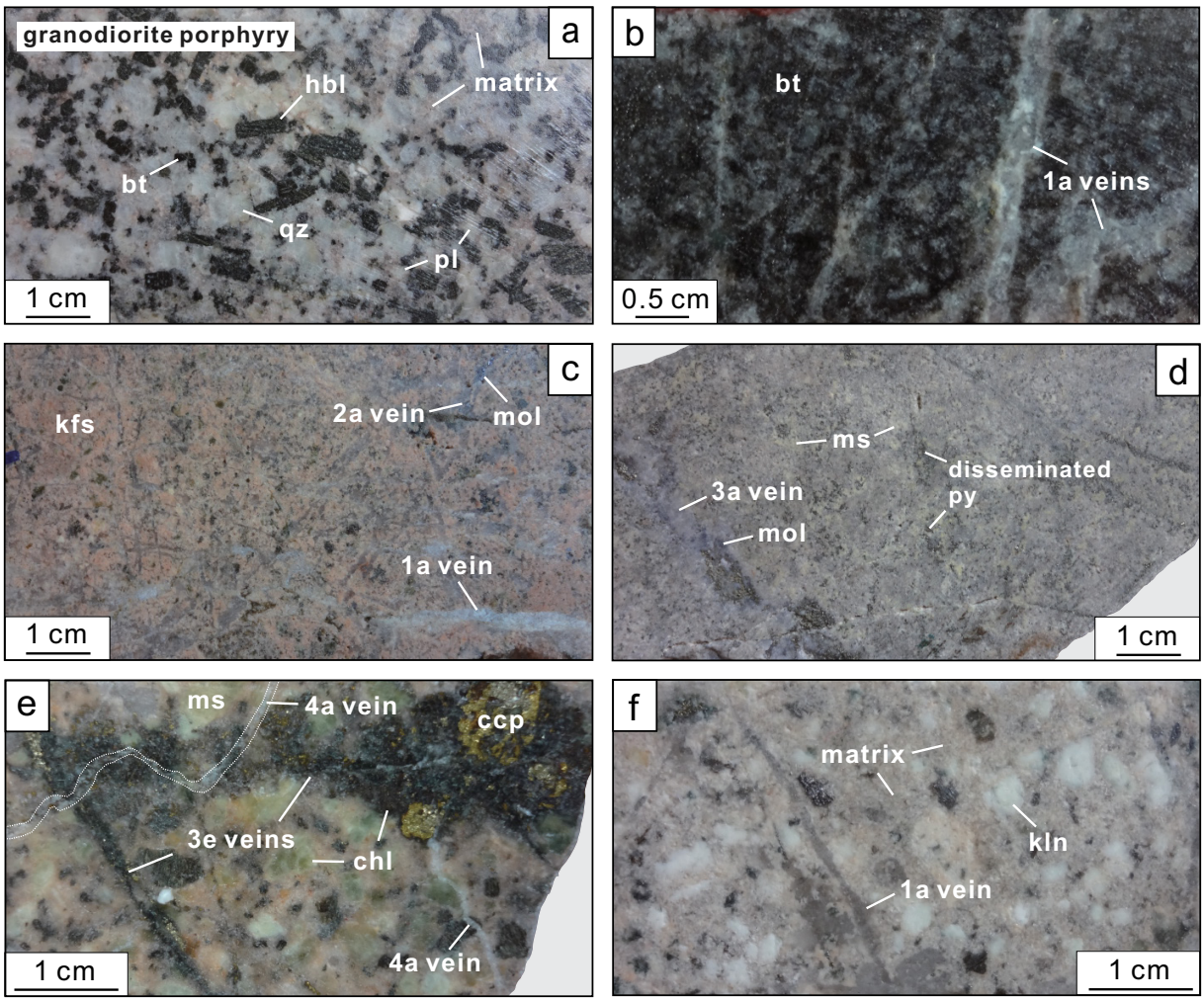

Fig. 3. Hand specimens showing lithologies and typical hydrothermal alteration types at Luoboling. (a) Fresh Luoboling granodiorite porphyry. (b) Biotite-magnetite altered the Luoboling granodiorite porphyry cut by stage 1a veins. (c) K-feldspar altered the Luoboling granodiotite porphyry with stage 1a and 2a veins. (d) Pyrite-quartz-muscovite altered the Luoboling granodiorite porphyry cut by stage 3a veins. (e) K-feldspar altered the Sifang granodiorite overprinted by chlorite-muscovite alteration and cut by stage 3e and 4c veins. Secondary K-feldspar was replaced by chlorite and muscovite. (f) Kaolinite altered the Luoboling granodiorite porphyry with stage 1a veins. Plagioclase phenocrysts were replaced by kaolinite. Abbreviations: bt = biotite, ccp = chalcopyrite, chl = chlorite, hbl = hornblende, kfs = K-feldspar, kln = kaolinite, mol = molybdenite, ms = muscovite, pl = plagioclase, py = pyrite, qz = quartz.

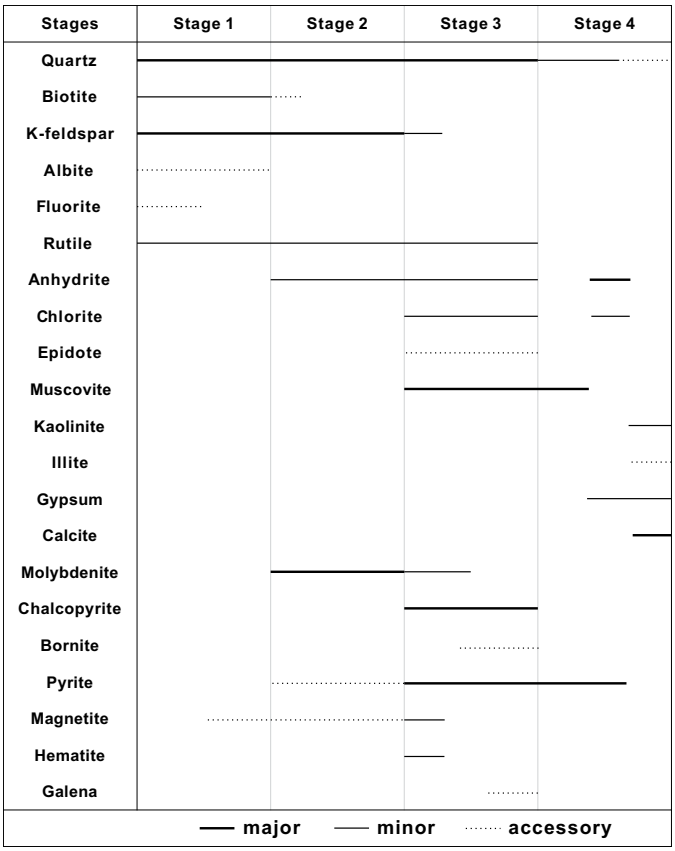

Fig. 4. Paragenetic sequence of ore and gangue minerals at Luoboling.

in the lower part of the deposit (Luoboling pluton; Fig. 2) and variably present irregular to straight textures. These veins are associated with potassic alteration and manifest as K-feldspar–dominant alteration halos (Fig. 5c, f) and minor biotite alteration halos (Fig. 4b). Hydrothermal K-feldspar and biotite occur locally in quartz veins. Limited fluorite and magnetite have occasionally been observed in the veins and alteration halos, respectively.

The Mo mineralization stage (stage 2) is characterized by abundant molybdenite-bearing quartz veins (Fig. 5d-f; Table 2) and is best developed in the lower part of the deposit (Luoboling pluton; Fig. 2). These veins generally cut stage 1 quartz veins (Fig. 5f). Molybdenite is the only sulfide mineral and typically crystallized along the margin of quartz veins (Fig. 5d, f). Anhydrite occurs in nearly 50% of the quartz-molybdenite veins (Fig. 5d) and locally occurs as independent anhydrite veins (Fig. 5g). Almost all stage 2 veins are accompanied by K-feldspar alteration halos.

Stage 3 is the Cu-Mo mineralization stage (Table 2). It produced multiple substages of chalcopyrite-bearing veins that have been subdivided into stages 3a-d on the basis of their mineral assemblages (Fig. 5h-l; Table 2). Chalcopyrite-bearing veins are concentrated in the middle to upper parts of the deposit (Luoboling and Sifang plutons; Fig. 2). Apart from a few stage 3a veins that have K-feldspar alteration halos, most of the stage 3 veins are associated with muscovite or chlorite-muscovite alteration (Fig. 5i-l). Chalcopyrite is the dominant sulfide, but molybdenite is also common (Fig. 5j). Anhydrite has been observed in stage 3a to 3d veins (Fig. 5l), whereas magnetite and hematite have been observed in stage 3c veins (Fig. 5i). Galena is rare and only occurs in stage 3b veins.

The late-mineralization stage (stage 4) is distinguished by abundant quartz-pyrite veins and minor calcite- and gypsum-bearing veins that lack chalcopyrite or molybdenite (Fig. 5m-p; Table 2). The quartz-pyrite veins have been subdivided into stages 4a-1 and 4a-2. Stage 4a-1 veins (Fig. 5m) are distributed in the middle to lower parts of the deposit (Luoboling pluton; Fig. 2), whereas stage 4a-2 veins (Fig. 5n) associated with intense quartz-muscovite alteration are concentrated at the top of the deposit (Luoboling and Sifang plutons; Fig. 2). Minor stage 4b veins (Fig. 5o) occur at the top of the orebodies, whereas stage 4c veins (Fig. 5p) have been observed throughout the deposit (Fig. 2).

Samples and Methods

A total of 157 samples representing different mineralization stages and alteration zones were collected from seven drill holes at elevations ranging from –387 to 585 m (Fig. 2). Thirty-five samples containing quartz phenocrysts and quartz-bearing veins were used to conduct SEM-CL analysis. A subset of 27 samples was selected for petrographic and microthermometric studies of fluid inclusions, and 25 samples were selected for LA-ICP-MS analysis of individual fluid inclusion compositions. All analyses were completed at the State Key Laboratory of Ore Deposit Geochemistry (SKLODG), Institute of Geochemistry, Chinese Academy of Science (IGCAS) in Guiyang.

SEM-CL imaging of quartz

SEM-CL analyses of quartz were performed using a JSM-7800F-type thermal field scanning electron microscope equipped with a Mono CL4 cathodoluminescence spectroscope. After the carbon-coating of slices, CL images were acquired under an acceleration voltage of ~10 kV and a beam current density of ~10 Na/mm.

Microthermometry of fluid inclusions

A Linkam THMSG600 cooling-heating stage was used for microthermometric analysis of fluid inclusions. The cooling-heating stage was calibrated at –56.6°, 0.0°, and 374.1°C using synthetic fluid inclusions. The precisions of temperature measurements were ±0.1° and ±2°C during freezing and heating, respectively. A heating rate lower than 0.1°C/s was used to obtain the ice-melting temperature, and the heating rate for the homogenization temperature was no more than 1°C/s when approaching the phase transition. Fluid inclusion data were acquired only on fluid inclusion assemblages to avoid accidental deviations (Goldstein and Reynolds, 1994). Irregular relict inclusions were also avoided to decrease the impact of postmodification. Due to the absence of CO_2-bearing inclusions, the salinity, density, and trapping pressure were calculated using the program HokieFlincs_H_2O-NaCl (Steele-MacInnis et al., 2012). The salinities of liquid-rich inclusions, vapor-rich inclusions, and intermediate-density inclusions (L, V, and ID type) were determined from corresponding ice-melting temperatures ($T_{m,\,ice}$) using the method of Bodnar (1993), and the salinities of brine inclusions (B type) were determined from halite

Table 1. Characteristics of Alteration Zones at Luoboling

Alteration zone	Major alteration minerals	Related mineralization and vein stages	Alteration styles	Spatial distribution
K-feldspar-biotite	Kfs, bt, (mag, ab)	Major Mo, minor Cu; 1a, 1b, 2a, 3a veins	Intensely developed; dominated by secondary K-feldspar and minor biotite, with vein halos up to 2 cm; intensely overprinted by phyllic alteration	Central region of the Luoboling pluton; deepest parts of the deposit
Quartz-muscovite	Qz, ms, (chl)	Major Cu, minor Mo; 3a, 3b, 3c, 3d, 4a veins	Intense and pervasive; dominated by fine-grained muscovite and quartz; the widest spatial distance; vein halos up to 1.5 cm	Within the Luoboling pluton; adjacent to and shallower than the K-feldspar-biotite alteration zone; middle parts of the deposit
Chlorite-muscovite	Chl, ep, ms, qz	Major Cu, minor Mo; 3a, 3b, 3d, 3e, 4b veins	Locally intense, spatially limited; vein halos up to 1.2 cm; chlorite and muscovite replaced phenocrysts	Along the northeastern margin of the Luoboling pluton; partly within the Sifang pluton; upper parts of the deposit
Kaolinite-pyrite-muscovite	Kln, py, qz, ms, ilt	Barren; 4a, 4c veins	Pervasive; vein halos are unclear; pyrite is disseminated; kaolinite and muscovite replaced phenocrysts	Mainly developed in the Sifang pluton, above the orebodies; adjacent to and shallower than the chlorite-muscovite alteration zone
Quartz-dickite	Qz, dck, kln, (prl)	Barren	Pervasive; spatially limited; rare veins; fine-grained dickite replaced secondary muscovite	Only developed in the Sifang pluton, northeastern region of the Luoboling pluton; above the deposit; near surface
Quartz-alunite-dickite	Qz, alu, dck, (kln, prl)	Barren	Pervasive; rare veins; unclear relationship with Luoboling	Only developed in the Sifang pluton, western region of the deposit; spatially associated with the Zijinshan high-sulfidation Cu-Au deposit

Mineral abbreviations: ab = albite, alu = alunite, bt = biotite, chl = chlorite, dck = dickite, ep = epidote, ilt = illite, kfs = K-feldspar, kln = kaolinite, mag = magnetite, ms = muscovite, prl = pyrophyllite, py = pyrite, qz = quartz

dissolution temperatures ($T_{m,\ NaCl}$) using the algorithm of Sterner et al. (1988).

LA-ICP-MS analyses of individual fluid inclusions

Major and trace element analyses of fluid inclusions from quartz phenocrysts and vein quartz were conducted using an Agilent 7900 ICP-MS equipped with a GeoLasPro 193-nm ArF excimer laser. A laser repetition of 8 Hz and an energy density of 10 J/cm^2 were used during the analyses. Laser spot sizes of 16 to 32 μm were used, depending on the sizes and depths of inclusions. NIST RAM610 was used as an external standard and analyzed twice every 10 spots. Weight percent NaCl equivalent concentrations of fluid inclusions obtained from microthermometry were used as internal standards (Heinrich et al., 2003). The charge-balance method was adopted to correct the modeled amounts of Na (from wt % NaCl equiv) for the salinity contributions of other cations, generally including K, Ca, Mn, Fe, Cu, Zn, and Pb. The corrected Na concentrations transformed the relative element concentrations into absolute values. More details are described in Lan et al. (2017, 2018). The original LA-ICP-MS data were reduced using the SILLS software (Guillong et al., 2008). As a result of difficulty in obtaining the precise salinity of every individual vapor inclusion that was selected for LA-ICP-MS analysis, approximately one-third of the tested vapor inclusions adopted the average salinity of the corresponding fluid assemblage as internal standards. Similarly, approximately 20% of brine and liquid-rich inclusions adopted average values. This approach may have increased uncertainty 3 to 25% for vapor and liquid-rich inclusions and <6% for brine inclusions.

Results

SEM-CL images

Primary coarse-grained quartz phenocrysts and stage 1a and 1b quartz veins have the highest and most homogeneous CL intensities in all quartz types (Fig. 6a, b). No internal growth zonation has been observed in these quartz grains. In some samples, stage 1a veins have been crosscut or reopened by stage 3a, 3b, 4a, or 4b veins containing CL-gray quartz and sulfides (Fig. 6a, b). These reactivated stage 1a veins can easily be misidentified as late-stage sulfide-bearing veins. In a few vein samples, stage 1 quartz grains have been strongly eroded and overgrown by later CL-dark quartz and locally formed residual CL-brighter cores (Fig. 6h). CL-black quartz forms thin rims along quartz grain boundaries and is probably due to postmineralization fluids.

Similar to stage 1, stage 2a veins are dominated by coarse-grained CL-bright quartz (Fig. 6c, d), which are associated with molybdenite (Fig. 6d). Weak CL-intensity heterogeneity occurs locally in specific quartz grains (Fig. 6c). Later-stage

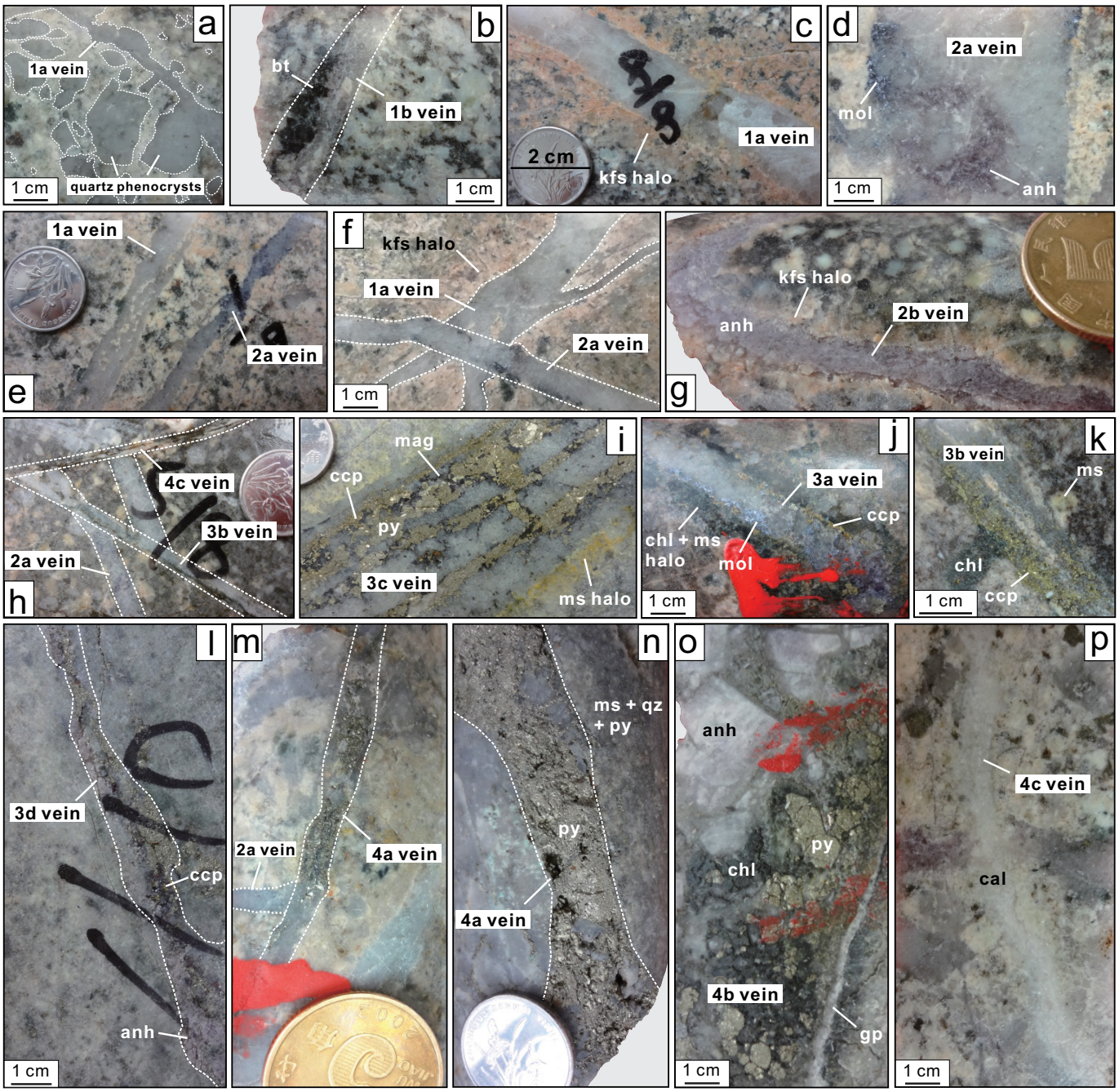

Fig. 5. Hand specimens showing different veins, mineralization, and related alteration types at Luoboling. (a) Quartz phenocrysts and irregular stage 1a vein. (b) Stage 1b vein with biotite alteration. (c) Barren stage 1a vein with K-feldspar halo. (d) Anhydrite-bearing stage 2a vein. (e) Coexisting stage 1a and 2a veins. (f) Irregular stage 1a vein with K-feldspar halo cut by stage 2a vein. (g) Stage 2b anhydrite vein with thin K-feldspar halo. (h) Stage 2a vein cut by stage 3b vein, with both cut by stage 4c vein. (i) Stage 3c vein with muscovite alteration halo. (j) Stage 3a vein with chlorite-muscovite alteration halo. (k) Stage 3b vein with chlorite-muscovite alteration. (l) Anhydrite-dominated stage 3d vein. (m) Stage 2a vein cut by deep-seated stage 4a-1 vein. (n) Shallow-seated stage 4a-2 vein in intense quartz-muscovite alteration zone. (o) Stage 4b vein cut by stage 4c vein. (p) Stage 4c vein with kaolinite alteration. Abbreviations: anh = anhydrite, bt = biotite, cal = calcite, ccp = chalcopyrite, chl = chlorite, gp = gypsum, kfs = K-feldspar, mag = magnetite, mol = molybdenite, ms = muscovite, py = pyrite, qz = quartz.

anhydrite and CL-dark quartz have formed the stockworks that overprinted the CL-bright stage 2a quartz (Fig. 6c).

Stage 3 veins are dominated by medium- to fine-grained CL-gray quartz, with lower CL intensities relative to quartz in stage 1 and stage 2 veins (Fig. 6e, f). These quartz grains are generally characterized by internal CL-dark cores, strong intensity heterogeneity, and immature growth zonation. All chalcopyrite and molybdenite grains in stage 3 veins are

Table 2. Vein Types at Luoboling

Vein type	Mineral assemblage	Alteration halo (width)	Thickness or diameter	Texture	Position	Crosscutting relationships	Abundance		Veins	Fluid inclusion type (%)			
							Mo	Cu		ID	V	B	L
Stage 1 (premineralization)													
Quartz phenocryst	Qz	–	0.3–2 cm	Irregular grains of different sizes; locally transform into irregular 1a veins	Within the Luoboling pluton; lower parts of the deposit	–	–	–	C	–	90	6	4
1a	Qz-(kfs, fl)	Kfs (≤10 mm)	2–12 cm	Irregular, straight or locally discontinuous veins with parallel to subparallel walls	Within the Luoboling pluton; lower to middle parts of the deposit	Cut feldspar phenocrysts		–	A	<1	90	6	4
1b	Qz-bt	Bt, (mag) (≤4 mm)	0.5–3 cm	Straight veins with parallel to subparallel walls	Within the Luoboling pluton; deep level of the deposit	–	–	–	R	–	–	–	–
Stage 2 (Mo mineralization)													
2a	Qz-mol-(anh, py)	Kfs, (bt) (≤5 mm)	0.2–5 cm	Straight, irregular or wavy veins with parallel walls	Within the Luoboling pluton; lower to middle parts of the deposit	Cut 1a veins	A	–	A	–	80	15	5
2b	Anh	Kfs (~4 mm)	1–2 cm	Wavy veins with parallel walls	Within the Luoboling pluton; middle parts of the deposit	Cut 1a veins	–	–	R	–	–	–	–
Stage 3 (Cu-Mo mineralization)													
3a	Qz-ccp-mol-py-(anh)	Kfs (≤6 mm) ms, qz, chl (≤8 mm)	0.5–3 cm	Straight veins with parallel walls	Within the Luoboling pluton; middle to upper parts of the deposit	Cut 1a and 2a veins	C	A	A	-	50	45	5
3b	Qz-ccp-py-(anh, gn)	Ms, chl, qz (≤8 mm)	0.5–4 cm	Straight veins with parallel walls	Within the Luoboling pluton; middle to upper parts of the deposit	Cut 1a and 2a veins	–	A	A	–	50	45	5
3c	Qz-py-ccp-mag-hem-(mol, anh)	Ms, qz (≤15 mm)	3–10 cm	Straight veins with parallel walls	Within the Luoboling and Sifang plutons; middle to upper parts and southeastern margin of the deposit	Cut 2a veins	R	C	C	–	70	20	10
3d	Anh-ccp-py	Qz, ms, chl (≤12 mm)	0.5–7 cm	Straight veins with parallel to subparallel walls	Within the Luoboling and Sifang plutons; southeastern margin of the deposit	–	–	R	R	–	–	–	–
3e	Ccp-py-chl	Chl, ep (≤3 mm)	0.1–1 cm	Straight veinlets	Within the Luoboling pluton; lower, middle to upper parts of the deposit	Cut 1a, 2a, and 3a veins	–	R	C	–	–	–	–
Stage 4 (late mineralization)													
4a-1	Qz-py	–	1–1.5 cm	Straight veins with subparallel walls	Within the Luoboling pluton; middle to lower parts of the deposit	Cut 2a and 3a veins	–	–	R		60	20	20
4a-2	Qz-py	Ms, qz (≤15 mm)	1–5 cm	Winding to straight veins with parallel walls	Within the Luoboling and Sifang plutons; top of the deposit	–	–	–	A	20	40	20	20
4b	Qz-anh-gp-chl-py	–	5–12 cm	Straight veins with parallel to subparallel walls	Within the Luoboling and Sifang plutons; periphery and upper parts of the deposit	–	–	–	R	–	20	–	80
4c	Cal-gp-(qz)	–	1–2 cm	Curving veins with unclear parallel walls	Within the Luoboling pluton; lower, middle to upper parts of the deposit	Cut 1a, 2a, 3a, and 3b veins	–	–	C	–	–	–	–

Mineral abbreviations: anh = anhydrite, bt = biotite, cal = calcite, ccp = chalcopyrite, chl = chlorite, ep = epidote, fl = fluorite, gn = galena, gp = gypsum, hem = hematite, kfs = K-feldspar, kln = kaolinite, mag = magnetite, mol = molybdenite, ms = muscovite, py = pyrite, qz = quartz
Abundance: A = abundant, C = common, R = rare
Fluid inclusion type: B = brine inclusion, ID = intermediate-density fluid inclusion, L = liquid-rich inclusion, V = vapor-rich inclusion
– = not observed

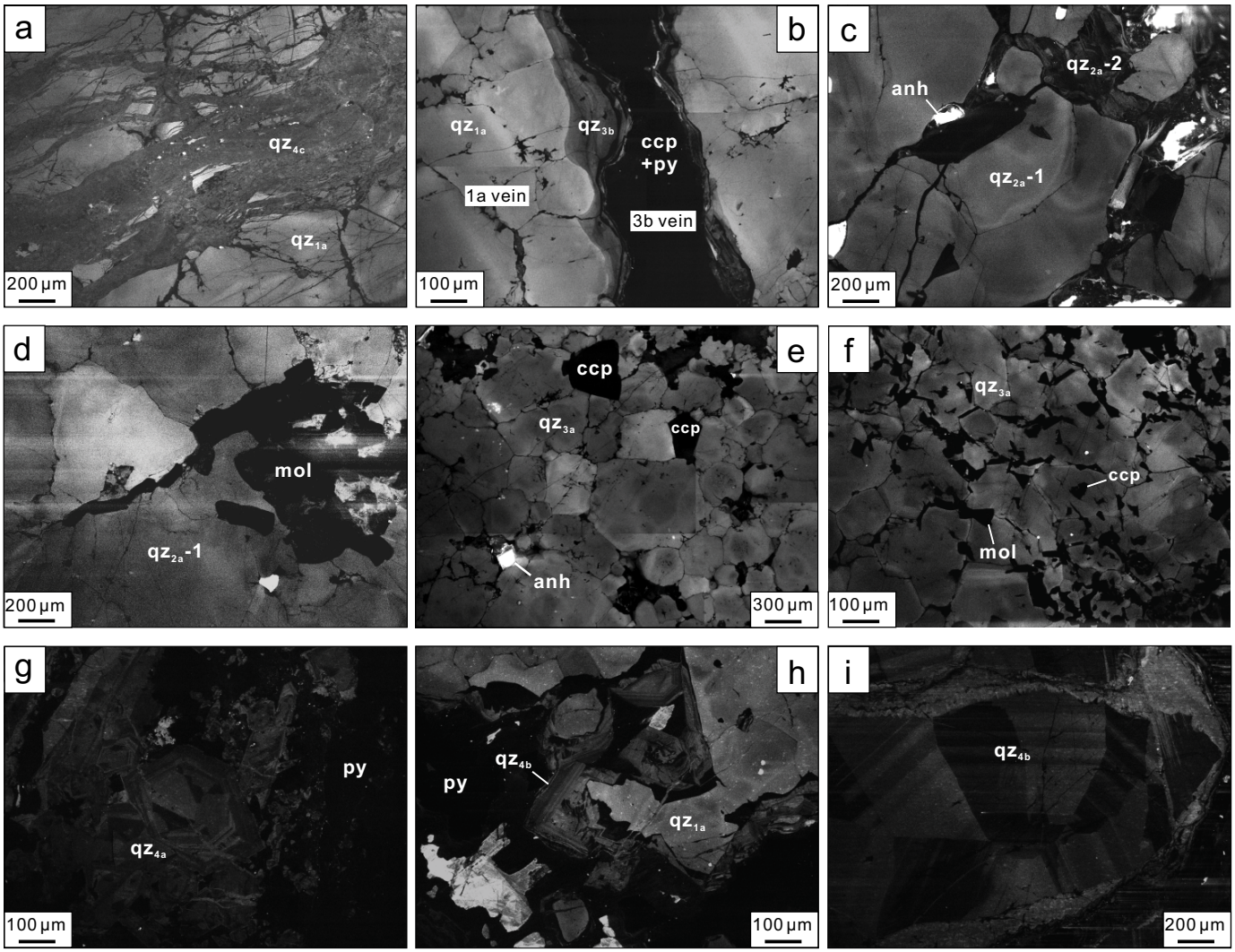

Fig. 6. SEM-CL images of quartz veins. (a) Stage 1a vein with CL-bright quartz cut by stage 4b vein with CL-dark quartz. (b) Stage 1a vein reopened by stage 3b vein with CL-gray quartz. (c) CL-bright quartz in stage 2a vein overprinted by quartz-anhydrite stockworks with CL-dark quartz. (d) Molybdenite coexisting with CL-bright quartz in stage 2a vein. (e) Chalcopyrite coexisting with fine-grained CL-gray quartz in stage 3a vein, where quartz displays dark cores or immature growth zonations. (f) Fine-grained chalcopyrite and molybdenite coexisting with fine-grained CL-gray quartz in stage 3a vein. (g) Pyrite coexisting with fine-grained CL-dark growth zoned quartz in stage 4a vein. (h) Quartz in stage 1a vein eroded and reopened by later stage 4b vein. (i) Coarse-grained quartz with perfect growth zonations in stage 4b vein. Abbreviations: anh = anhydrite, ccp = chalcopyrite, mol = molybdenite, py = pyrite, qz = quartz.

intergrown with this quartz type (Fig. 6e, f). In contrast to the first two vein stages, stage 3 quartz is homogeneous, with no obvious subgenerations observed.

Very low CL intensity and good internal growth zonation characterizes both stage 4a and 4b quartz veins (Fig. 6g-i). Quartz in stage 4a veins is typically fine grained and anhedral, with discrete growth zones (Fig. 6g), whereas stage 4b quartz is coarse grained and euhedral and has the best-developed growth zones of all quartz types at Luoboling (Fig. 6i).

Fluid inclusion petrography

All fluid inclusions analyzed in this study were from fluid inclusion assemblages, including predominant inclusion groups and minor trails. Four major inclusion types have been distinguished according to phase types and ratios at room temperature, identified here as B, V, L, and ID type. This classification is mostly consistent with Zhong et al. (2014), with the addition of type ID inclusions. Type ID inclusions have vapor/liquid ratios between type V and type L inclusions at room temperature and are subdivided into IDV (homogenized to vapor) and IDL (homogenized to liquid) inclusions at stage 4. Laser Raman spectroscopic analyses indicate the presence of rare CO_2-bearing inclusions, consistent with Zhong et al. (2014). Only one fluid inclusion with visible CO_2 was observed in stage 2 veins at room temperature (Fig. 7k). The distribution of different inclusion types in different stage veins and their spatial locations are presented in Tables 2 and 3 and Figure 2. More detailed petrographic characteristics are summarized in Table 4.

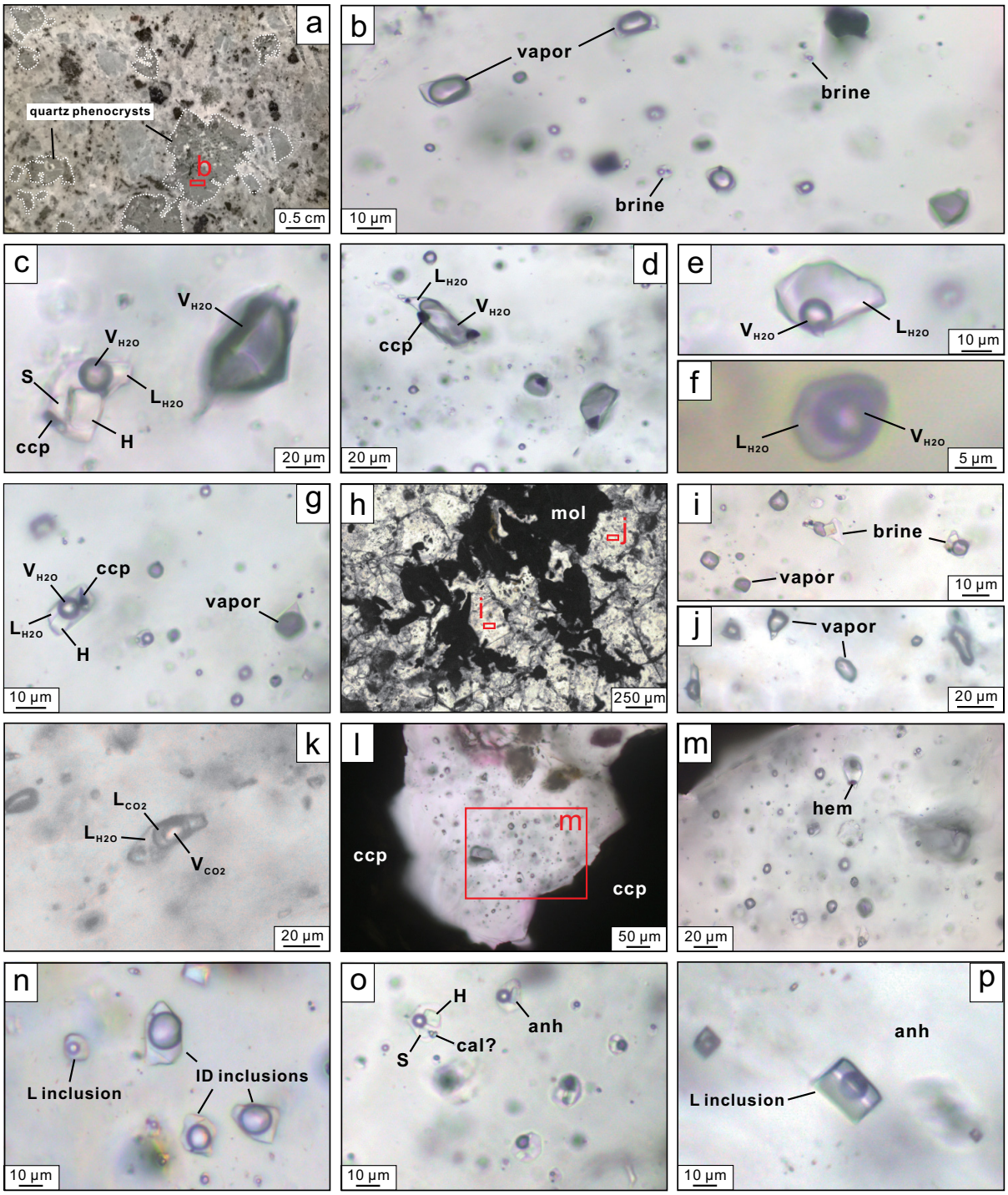

Fig. 7. Fluid inclusions in different stage quartz veins at Luoboling. (a) Fluid inclusion-bearing quartz phenocrysts in the Luoboling granodiorite porphyry. (b) Vapor-dominant fluid inclusion assemblage in quartz phenocryst in the Luoboling granodiorite porphyry. (c) Coexisting brine and vapor inclusions in quartz phenocryst in the Luoboling granodiorite porphyry. (d) Vapor-rich fluid inclusions with chalcopyrite daughter minerals in quartz phenocryst in the Luoboling granodiorite porphyry. (e) Liquid-rich fluid inclusion in stage 1a vein. (f) Extremely rare intermediate-density inclusion in deep-level stage 1a vein. (g) Brine inclusions coexisting with dominantly vapor-rich inclusions in deep-seated stage 1a vein. (h) Fluid inclusion-bearing quartz coexisting with molybdenite in stage 2a vein. (i) Coexisting vapor and brine inclusions and (j) vapor-rich inclusion assemblage in stage 2a vein. (k) Rare CO_2-bearing inclusion with double bubble in stage 2a vein. (l, m) Chalcopyrite surrounding coexisting vapor and brine inclusions in stage 3a vein. (n) Intermediate-density inclusions in stage 4a-2 vein. (o) Brine inclusions without chalcopyrite daughter minerals in stage 4a-2 vein. (p) Liquid-rich inclusions in anhydrite from stage 4b vein. Abbreviations: anh = anhydrite, cal = calcite, ccp = chalcopyrite, H = halite, hem = hematite, ID inclusion = intermediate-density inclusion, L inclusion = liquid-rich inclusion, L_{CO_2} = liquid CO_2, L_{H_2O} = liquid H_2O, mol = molybdenite, S = sylvite, V_{CO_2} = vapor CO_2, V_{H_2O} = vapor H_2O.

Table 3. Distribution of Fluid Inclusions in Samples Used for Microthermometry and LA-ICP-MS Analyses

Sample	Host rock and alteration	Vein type	Drill hole	Drill hole coordinates (UTM) E	N	Elevation (m)	Inclusion type (%) V	B	L	ID
LBL16-18	Luoboling granodiorite porphyry; kfs	Quartz phenocryst	36-272	443121	2788084	–124	90	5	5	
LBL18-2	Luoboling granodiorite porphyry; kfs	1a	36-282	443255	2788195	–314	92	6	2	
LBL16-22	Luoboling granodiorite porphyry; kfs	1a	36-272	443121	2788084	–103	90	6	4	
LBL16-26	Luoboling granodiorite porphyry; kfs	Quartz phenocryst	36-272	443121	2788084	–235	93	4	3	
LBL16-9	Luoboling granodiorite porphyry; kfs	1a	36-272	443121	2788084	–202	88	6	6	
LBL16-10	Luoboling granodiorite porphyry; kfs	2a	36-272	443121	2788084	–187	85	10	5	
LBL18-11	Luoboling granodiorite porphyry; bt	2a	36-282	443255	2788195	–263	82	14	4	
LBL16-22	Luoboling granodiorite porphyry; kfs	2a	36-272	443121	2788084	–95	80	12	8	
LBL16-17	Luoboling granodiorite porphyry; kfs-bt	2a	36-272	443121	2788084	–139	75	18	7	
LBL18-31	Luoboling granodiorite porphyry; kfs	2a	36-282	443255	2788195	–145	78	14	8	
LBL18-72	Luoboling granodiorite porphyry; kfs	2a	40-268	443073	2787896	–75	85	12	7	
LBL18-27	Luoboling granodiorite porphyry; kfs	2a	36-282	443255	2788195	–134	80	14	6	
LBL18-62	Luoboling granodiorite porphyry; kfs	2a	40-268	443073	2787896	–170	85	8	7	
LBL16-6	Luoboling granodiorite porphyry; kfs-bt	3a	36-272	443121	2788084	–217	50	45	5	
LBL16-29	Luoboling granodiorite porphyry; chl-ms	3a	36-272	443121	2788084	50	60	32	8	
LBL18-102	Luoboling granodiorite porphyry; qz-ms	3c	56-264	443272	2787674	–133	75	20	5	
LBL18-110	Sifang granodiorite; qz-ms	3c	56-264	443272	2787674	97	70	15	15	
LBL18-109	Sifang granodiorite; qz-ms	3c	56-264	443272	2787674	–97	70	18	12	
LBL18-30	Luoboling granodiorite porphyry; qz-ms	3b	36-282	443255	2788195	–82	50	45	5	
LBL18-42	Sifang granodiorite; qz-ms	3b, 4a-1	36-282	443255	2788195	57	48	45	7	
LBL16-32	Luoboling granodiorite porphyry; chl-ms	3a	36-272	443121	2788084	19	55	38	7	
LBL18-92	Sifang granodiorite; qz-ms	4a-2	VIII02	442873	2787720	388	40	25	15	20
LBL16-25	Luoboling granodiorite porphyry; ms	4a-1	36-272	443121	2788084	81	60	20	20	
LBL18-94	Luoboling granodiorite porphyry; qz-py-ms	4a-2	VIII02	442873	2787720	338	35	20	20	25
LBL18-86	Sifang granodiorite; qz-ms	4a-2	VII01	442862	2787865	506	45	15	20	20
LBL16-47	Sifang granodiorite; chl-ms	3a, 4b	36-272	443121	2788084	110	20		80	
LBL16-44	Sifang granodiorite; chl-qz-ms	4b	36-272	443121	2788084	151	15		85	

Mineral abbreviations: bt = biotite, chl = chlorite, kfs = K-feldspar, ms = muscovite, py = pyrite, qz = quartz
Fluid inclusion type: B = brine inclusion, ID = intermediate-density inclusion, L = liquid-rich inclusion, V = vapor-rich inclusion

Table 4. Petrographic Characteristics of Fluid Inclusions from Luoboling

Stage	Type	Size and shape	Vol % bubble	Major daughter minerals	CL style of host quartz
Stage 1	V	10–40 μm; negative crystal to irregular	70–95	Abundant ccp	Coarse-grained; CL-bright, with homogeneous CL intensity
	B	8–20 μm; negative crystal	15–35	Hl, syl, anh, hem, other salts, ccp	
	L	5–20 μm; negative crystal	15–25	Occasional ccp	
	ID (<1%)	10–15 μm, negative crystal	40–60	None	
Stage 2	V	8–20 μm; negative crystal to irregular	80–95	Abundant ccp	Coarse-grained; CL-bright, with homogeneous CL intensity; associated with molybdenite
	B	3–12 μm; negative crystal to irregular	25–35	Hl, syl, anh, ccp	
	L	5–15 μm; negative crystal	10–30	Occasional ccp	
Stage 3	V	5–25 μm; negative crystal	85–100	Common ccp	Medium- to fine-grained; CL-gray, with CL intensity heterogeneity and immature growth zonations; associated with molybdenite and chalcopyrite
	B	4–23 μm; negative crystal to irregular	8–30	Hl, syl, hem, ccp	
	L	5–15 μm; negative crystal	18–30	Occasional ccp	
Stage 4	V	8–23 μm; negative crystal	85–100	Occasional ccp or none	Fine- or coarse-grained; CL-dark, with well-developed growth zonations; associated with pyrite in stage 4a veins
	B	3–15 μm; negative crystal	10~15	Hl, syl, anh, hem, cal	
	L	5–18 μm; negative crystal	5–30	None	
	ID IDV	8–12 μm; negative crystal	50–65	None	
	ID IDL	5–12 μm; negative crystal	45–60	None	

Mineral abbreviations: anh = anhydrite, cal = calcite, ccp = chalcopyrite, hem = hematite, hl = halite, syl = sylvite
Fluid inclusion type: B = brine inclusion, ID = intermediate-density fluid inclusion, IDL = intermediate-density fluid inclusion homogenizing to liquid, IDV = intermediate-density fluid inclusion homogenizing to vapor, L = liquid-rich inclusion, V = vapor-rich inclusion

Microthermometry

A total of 383 fluid inclusions were analyzed from 72 fluid inclusion assemblages. The samples used for microthermometry and LA-ICP-MS analysis of fluid inclusions are summarized in Table 3. Microthermometry results are presented in Table 5 as averages of fluid inclusion assemblages with 1σ uncertainty and in Figure 8 and Appendix 1 as complete data.

Stage 1: Type L inclusions in stage 1 quartz phenocrysts and veins homogenized to liquid between 326° and 436°C. Ice-melting temperatures of 85% of type L inclusions are between –1.4° and –9.7°C, with corresponding salinities between 2.4 and 13.6 wt % NaCl equiv. All type B inclusions homogenized to liquid after halite dissolution during the heating process. Halite dissolution temperatures range from 358° to 545°C, and vapor bubbles disappeared between 541° and >600°C. Around 50% of type B inclusions have final homogenization temperatures higher than 600°C (upper limit of cooling-heating stage). Salinities between 42.6 and 65.8 wt % NaCl equiv were calculated from halite dissolution temperatures. Type V inclusions homogenized to vapor between 474° and >600°C. Their ice-melting temperatures were between –2.5° and –7.3°C, reflecting salinities of 4.2 to 10.9 wt % NaCl equiv.

Stage 2: Type L inclusions in stage 2 veins homogenized to liquid between 355° and 415°C. Their ice-melting temperatures are between –1.9° to –5.4°C, corresponding to salinities of 3.2 to 8.4 wt % NaCl equiv. Among type B inclusions, 30% homogenized by halite dissolution at 394° to 461°C, with L-V homogenization at 337° to 398°C, corresponding to salinities between 47.3 and 54.6 wt % NaCl equiv. A total of 70% of type B inclusions homogenized by vapor bubble disappearance at 445° to 554°C, with final halite dissolution occurring between 333° and 492°C, corresponding to calculated salinities of 40.7 to 58.3 wt % NaCl equiv. Type V inclusions homogenized to vapor between 405° and 477°C. Ice-melting temperatures of –2.1° to –6.7°C correspond to salinities of 3.5 to 10.1 wt % NaCl equiv.

Stage 3: Type L inclusions in stage 3 veins homogenized to liquid between 324° and 385°C. Ice-melting temperatures of –1.2° to –2.9°C imply salinities from 2.1 to 4.8 wt % NaCl equiv. More than 60% of type B inclusions in stage 3 homogenized by final halite dissolution at temperatures between 332° and 465°C, corresponding to salinities of 41.2 to 54.5 wt % NaCl equiv, whereas vapor homogenization occurred between 215° and 371°C. The remaining type B inclusions homogenized to liquid by vapor disappearance at 332° to 471°C, and halite dissolution occurred at 311° to ~414°C, reflecting salinities from 38.9 to 48.9 wt % NaCl equiv. Type V inclusions homogenized to vapor from 312° to 438°C, with ice-melting temperatures of –0.6° to –5.8°C, corresponding to salinities between 1.1 and 8.9 wt % NaCl equiv.

Stage 4: Type L inclusions in stage 4a veins homogenized to liquid between 340° and 402°C. Ice-melting temperatures of –0.6° to –1.9°C imply salinities from 1.1 to 3.2 wt % NaCl equiv.

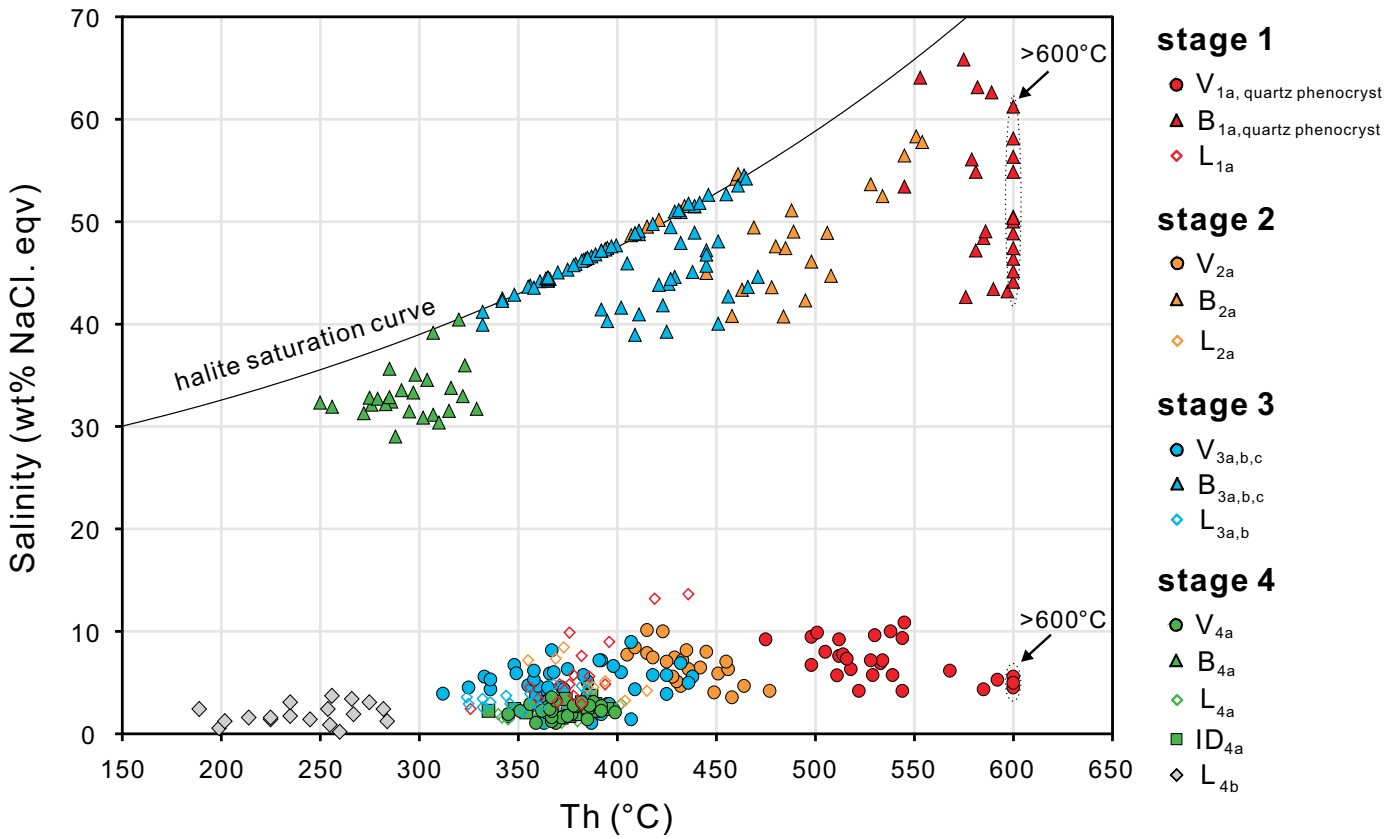

Fig. 8. Summary plot of microthermometric results for all fluid inclusion types. All data are presented in Appendix 1.

Table 5. Microthermometry Data for Fluid Inclusion Assemblages

Assemblages	Boiling assemblage	Vein type	Inclusion type (*n*)	$T_{m,ice}$ (°C)	S.D.	$T_{m,NaCl}$ (°C)	S.D.	Th (°C)	S.D.	Salinity (wt % NaCl equiv)	S.D.
Stage 1											
LBL16-18-3	Yes	Phenocryst	L (3)	–1.6	0.2			359	29	2.8	0.3
LBL16-26-3	Yes	1a	L (3)	–5.7	0.9			385	10	8.8	1.1
LBL16-22-2		Phenocryst	L (2)	–9.5	0.3			428	12	13.4	0.3
LBL18-2-3		1a	L (5)	–2.5	0.4			368	10	4.2	0.7
LBL16-22-3		1a	L (3)	–3.3	0.3			386	8	5.4	0.5
LBL18-2-1		1a	V (7)	–4.1	0.5			524	10	6.6	0.7
LBL16-22-1		1a	V (3)	–6.2	0.3			491	14	9.5	0.3
LBL16-22-4		1a	V (6)	–3.0	0.5			>566		4.9	0.7
LBL16-18-2	Yes	Phenocryst	V (3)	–3.1	0.6			>584		5.2	0.9
LBL16-9-2		1a	V (5)	–6.5	0.5			534	14	9.8	0.7
LBL18-2-2	Yes	1a	V (4)	–4.7	0.4			508	8	7.4	0.6
LBL16-22-1		1a	B (4)			366	7	>591		43.3	0.6
LBL16-18-2	Yes	Phenocryst	B (5)			529	11	>580		63.4	1.7
LBL16-18-3	Yes	1a	B (3)			428	6	>595		49.8	0.7
LBL16-9-1		1a	B (6)			474	13	>584		55.6	1.6
LBL16-26-2	Yes	Phenocryst	B (3)			395	9	>594		46.2	1.0
LBL18-2-2	Yes	1a	B (4)			419	11	>596		49.3	1.4
Stage 2											
LBL16-17-2		2a	L (5)	–2.6	0.4			397	12	4.3	0.7
LBL16-10-2	Yes	2a	L (3)	–4.8	0.5			366	9	7.6	0.7
LBL18-31-1		2a	V (4)	–4.5	0.6			441	17	7.1	0.8
LBL18-72-2		2a	V (4)	–3.5	0.4			438	11	5.7	0.6
LBL18-27-1		2a	V (3)	–6.2	0.8			424	10	9.4	1.1
LBL16-10-1	Yes	2a	V (6)	–4.8	0.4			420	11	7.5	0.5
LBL16-17-1	Yes	2a	V (5)	–2.5	0.3			456	17	4.2	0.5
LBL16-10-3		2a	B (3)			353	21	496	12	42.6	2.0
LBL16-10-1	Yes	2a	B (4)			360	19	461	14	43.2	1.7
LBL18-62-1	Yes	2a	B (3)			417	16	493	11	49.1	1.9
LBL16-22-1		2a	B (5)			406	12	406	12	48.6	1.4
LBL18-11-3	Yes	2a	B (4)			476	20	546	9	56.3	2.6
LBL18-31-2		2a	B (4)			423	23	491	26	50.3	2.6
LBL16-17-1	Yes	2a	B (4)			435	34	435	34	51.6	3.9
Stage 3											
LBL16-6-3	Yes	3a	L (5)	–2.0	0.2			332	8	3.3	0.3
LBL16-47-1		3a	L (5)	–1.5	0.2			350	11	2.6	0.4
LBL16-29-3	Yes	3a	L (4)	–2.6	0.3			373	13	4.4	0.4
LBL18-42-3		3b	V (3)	–2.5	0.2			324	12	4.2	0.3
LBL18-30-4		3b	V (2)	–1.2	0.3			350	7	2.1	0.5
LBL18-102-2		3c	V (4)	–3.2	0.6			370	11	5.2	0.9
LBL18-109-2	Yes	3c	V (6)	–1.5	0.4			375	8	2.6	0.6
LBL18-102-3		3c	V (3)	–1.5	0.2			395	4	2.6	0.3
LBL18-30-2		3b	V (6)	–4.5	0.7			404	15	7.1	1.0
LBL18-110-2		3c	V (4)	–0.8	0.2			387	18	1.4	0.4
LBL18-30-1	Yes	3b	V (3)	–2.2	0.5			410	15	3.7	0.7
LBL16-29-6	Yes	3a	V (6)	–4.0	0.7			357	15	6.4	1.0
LBL16-29-7	Yes	3a	V (4)	–3.1	0.4			429	9	5.5	0.4
LBL16-29-4	Yes	3a	V (7)	–2.6	0.4			370	11	4.4	0.7
LBL16-6-4	Yes	3a	V (4)	–3.3	0.3			353	14	5.3	0.5
LBL18-102-1		3c	B (3)			322	6	424	28	39.8	0.5
LBL18-109-2		3c	B (5)			353	14	436	23	42.6	1.2
LBL18-102-2	Yes	3c	B (4)			368	14	408	8	44.0	1.4
LBL16-29-2	Yes	3b	B (4)			329	15	384	35	40.5	1.3
LBL16-32-4		3a	B (8)			387	32	387	32	45.6	1.4
LBL16-29-5	Yes	3a	B (4)			372	38	372	38	44.9	3.1
LBL16-32-3		3a	B (10)			389	21	424	42	46.4	1.7
LBL18-42-1		3a	B (9)			413	38	413	38	45.0	1.4
LBL16-6-1	Yes	3a	B (5)			378	13	378	13	45.6	1.4
LBL16-29-1	Yes	3b	B (5)			387	26	387	26	46.7	2.7
LBL18-42-4		3b	B (8)			414	37	414	37	49.8	2.7
LBL18-30-1	Yes	3b	B (6)			404	48	404	48	48.7	4.3
LBL18-42-2		3a	B (6)			381	12	381	12	46.1	1.2
LBL16-6-2	Yes	3b	B (4)			359	26	359	26	50.2	2.4

Table 5. *(Cont.)*

Assemblages	Boiling assemblage	Vein type	Inclusion type (*n*)	$T_{m, ice}$ (°C)	S.D.	$T_{m,NaCl}$ (°C)	S.D.	Th (°C)	S.D.	Salinity (wt % NaCl equiv)	S.D.
Stage 4											
LBL16-25-5		4a-1	L (3)	–0.6	0.1			372	8	1.1	0.1
LBL18-86-3		4a-2	L (4)	–1.4	0.3			390	15	2.5	0.5
LBL18-92-4		4a-2	L (7)	–1.6	0.2			374	7	2.7	0.4
LBL18-92-3		4a-2	L (6)	–1.1	0.2			349	8	1.9	0.4
LBL18-94-2		4a-2	IDL (1)	–1.3	–			335	–	2.2	–
			IDV (5)	–1.3	0.3			361	10	2.2	0.4
LBL18-94-3		4a-2	IDL (2)	–1.3	0.4			381	6	2.3	0.6
			IDV (4)	–1.4	0.3			388	7	2.4	0.4
LBL18-92-2		4a-2	IDL (3)	–2.0	0.2			381	7	3.4	0.3
LBL16-25-3		4a-1	V (7)	–1.7	0.3			376	12	2.9	0.4
LBL18-86-4		4a-2	V (4)	–1.3	0.3			363	17	2.1	0.4
LBL18-92-4		4a-2	V (6)	–0.8	0.2			372	9	1.4	0.3
LBL16-25-1		4a-1	V (6)	–1.4	0.3			372	9	2.4	0.5
LBL18-94-3		4a-2	V (6)	–1.4	0.2			379	16	2.5	0.4
LBL18-86-2		4a-2	B (8)			179	21	302	17	30.9	0.9
LBL16-25-2		4a-1	B (2)			206	7	271	21	32.2	0.3
LBL18-42-6		4a-1	B (6)			226	24	289	26	33.3	1.5
LBL16-25-4		4a-1	B (2)			212	9	276	1	32.5	0.5
LBL18-42-5		4a-1	B (2)			314	9	314	9	39.4	0.8
LBL18-92-2		4a-2	B (4)			229	6.0	307	15	33.4	0.3
LBL18-94-1		4a-2	B (4)			260	10	303	16	35.3	0.6
LBL16-44-3		4b	L (4)	–2.0	0.2			258	17	3.3	0.3
LBL16-47-1		4b	L (2)	–0.2	0.1			230	43	0.4	0.2
LBL16-44-2		4b	L (4)	–0.7	0.1			247	34	1.2	0.2
LBL16-44-1		4b	L (8)	–1.1	0.3			236	30	1.9	0.4

Fluid inclusion type: B = brine inclusion, IDL = intermediate-density inclusion homogenizing to liquid, IDV = intermediate-density inclusion homogenizing to vapor, L = liquid-rich inclusion, V = vapor-rich inclusion

– = not calculated, *n* = number of analyzed inclusions, S.D. = standard deviation, Th = final homogenization temperature, $T_{m, ice}$ = ice-melting temperature, $T_{m, NaCl}$ = halite dissolution temperature

All type B inclusions homogenized to liquid by final vapor disappearance, with vapor homogenization temperatures between 250° and 329°C, and halite dissolution temperatures from 133° to 320°C, corresponding to salinities between 29.0 and 40.4 wt % NaCl equiv. Type V inclusions homogenized to vapor at 345° to 399°C, with ice-melting temperatures of –0.6° to –2.1°C, corresponding to salinities between 1.1 and 3.5 wt % NaCl equiv. Type IDL inclusions homogenized to liquid at temperatures between 335° and 387°C, with ice-melting temperatures of –1.0° to –2.2°C, indicating salinities between 1.7 and 3.7 wt % NaCl equiv. Type IDV inclusions homogenized to vapor between 348° and 395°C, with ice-melting temperatures of –0.9° to –1.7°C, corresponding to salinities of 1.6 to 2.9 wt % NaCl equiv.

In stage 4b veins, type L inclusions were dominant and homogenized to liquid at 189° to 284°C. They have ice-melting temperatures between –0.1° and –2.2°C, corresponding to salinities from 0.2 to 3.7 wt % NaCl equiv.

Compositions of fluid inclusions

LA-ICP-MS analytical results for 245 individual inclusions from 52 inclusion assemblages are summarized in Table 6 as averages for assemblages with 1σ uncertainty. All data are presented in Appendix 2. Typical LA-ICP-MS signals of fluid inclusions are shown in Figure 9.

Type B inclusions have the highest concentrations of most elements analyzed from all vein stages and across all inclusion types. In stage 1, elements such as K and Fe have concentrations typically higher than 30,000 ppm. Cu and Mn have concentrations from thousands of parts per million to more than 10,000 ppm. Zn and Pb have concentrations generally between 1,000 and 5,000 ppm, whereas Rb, Sr, Mo, Ag, Cs, Ba, and W exhibit relatively lower concentrations from several to hundreds of parts per million (Table 6). The concentrations of Au, As, and Sn were generally below detection limits. The compositions of type B inclusions in stage 2 veins are similar to those in stage 1, apart from lower Mo concentrations (typically <15 ppm; Table 6). Type B inclusions in stage 3 veins are characterized by lower Cu concentrations (typically <5,000 ppm) compared with those from stage 1 and stage 2 (Table 6). Type B inclusions in stage 4a veins exhibit two different behaviors. Relative to type B inclusions from stage 1 to stage 3, type B inclusions in shallow-level stage 4a-2 veins display a lack of Mo (typically below detection limits), similar Cu (thousands of ppm), and higher concentrations of Pb (up to 8,800 ppm) and Zn (up to 13,000 ppm; Figs. 2b, c, 5n; Table 6), whereas type B inclusions in deep-level stage 4a-1 veins display a lack of Mo (typically below detection limits) and one to two orders of magnitude lower Cu contents (typically <500 ppm; Figs. 2b, 5m; Table 6).

Most elements, including K, Mn, Fe, Zn, Rb, Sr, Cs, Ba, W, and Pb, have one to two orders of magnitude lower concentrations in type V inclusions than those in type B inclusions from corresponding veins (Table 6). Copper is an exception; it has

Table 6. LA-ICP-MS Concentration Data for Fluid Inclusion Assemblages

Assemblages	Vein type	Inclusion type (*n*)		Na (wt %)	K (wt %)	Fe (wt %)	Mn (ppm)	Cu (ppm)	Zn (ppm)	Rb (ppm)	Sr (ppm)	Mo (ppm)	Ag (ppm)	Cs (ppm)	Ba (ppm)	W (ppm)	Pb (ppm)	Bi (ppm)
Stage 1																		
LBL16-22-1	1a	B (4)	Average	10	3.5	9.8	13,000	14,000	5,400	600	89	10	34	86	52	750	2,300	51
			S.D.	1.3	1.2	6.3	5,600	4,600	4,400	280	15	7.9	64	34	16	1,300	950	60
LBL16-9-1	1a	B (2)	Average	12	5.5	10.4	16,000	5,500	4,300	620	100	18	2.7	99	81	69	2,400	25
			S.D.	0.7	0.10	2.3	2,100	71	990	71	41	19	3.8	2.1	16	86	350	7.8
LBL16-18-2	Phenocryst	B (3)	Average	12	3.0	11	13,000	6,700	2,600	320	74	37	7.8	57	61	190	1,700	17
			S.D.	1.2	0.64	3.7	3,800	3,700	950	120	5.8	26	1.6	23	3.8	12	640	7.2
LBL18-2-2	1a	B (4)	Average	11	5.0	8.0	16,000	12,000	5,600	550	210	35	6.5	96	320	120	2,400	62
			S.D.	1.5	0.84	0.52	3,900	4,900	3,700	120	150	36	5.8	23	450	110	700	59
LBL18-2-1	1a	V (4)	Average	1.2	0.43	0.60	1,100	8,500	410	50	16	0.93	2.5	8.8	6.1	8.6	220	1.8
			S.D.	0.41	0.12	0.25	860	4,000	240	20	4.4	1.2	3.0	3.0	2.6	1.3	130	0.28
LBL18-2-2	1a	V (6)	Average	1.3	0.46	0.64	1,300	6,900	480	51	10	0.36	3.3	8.1	5.8	24	190	1.7
			S.D.	0.31	0.13	0.22	570	1,800	210	13	1.7	0.6	1.7	2.2	1.5	47	63	0.43
LBL16-22-1	1a	V (9)	Average	1.4	0.41	0.73	1,000	8,300	420	60	13	4.0	1.6	11	8.8	32	170	2.5
			S.D.	0.50	0.20	0.33	710	3,300	200	23	7.6	8.1	2.9	3.7	3.0	66	130	1.0
LBL16-9-2	1a	V (5)	Average	1.3	0.56	1.1	1,100	8,900	680	65	15	0.24	4.1	9.0	7.6	11	340	4.2
			S.D.	0.55	0.17	0.46	650	4,500	320	20	1.0	0.5	7.3	3.7	1.3	10	220	0.65
LBL16-18-2	Phenocryst	V (3)	Average	1.5	0.73	0.50	1,600	11,000	490	71	14	n.d.	4.0	12	8.3	8.9	270	4.2
			S.D.	0.45	0.17	0.16	557	8,188	166	12	6.7	–	6.9	3.4	4.1	0.35	84	3.2
LBL18-2-3	1a	L (4)	Average	0.49	0.13	0.39	410	5,000	310	19	4.8	n.d.	0.38	2.1	3.0	12	120	2.3
			S.D.	0.17	0.086	0.40	250	3,000	430	7.0	2.3	–	0.75	0.66	1.1	6.2	81	1.1
LBL16-22-3	1a	L (5)	Average	1.5	0.47	0.77	1,400	6,000	420	60	23	2.7	1.5	12	11	26	230	3.4
			S.D.	0.43	0.22	0.28	810	930	250	30	13	2.0	3.3	3.7	8.1	36	72	1.3
LBL16-26-3	1a	L (1)	Average	0.90	0.16	0.40	190	3,900	200	25	16	n.d.	n.d.	5.0	7.1	2.7	130	1.1
			S.D.	–	–	–	–	–	–	–	–	–	–	–	–	–	–	–
LBL16-18-3	Phenocryst	L (3)	Average	0.34	0.091	0.45	700	8,900	140	11	17	0.27	13	1.5	1.8	2.7	120	3.5
			S.D.	0.26	0.051	0.35	–	10,000	41	8.7	24	0.46	15	0.57	1.0	2.6	86	2.6
Stage 2																		
LBL16-10-1	2a	B (1)	Average	9.2	7.9	7.9	10,000	6,300	3,100	730	130	56	8.8	74	130	1,300	1,300	160
			S.D.	–	–	–	–	–	–	–	–	–	–	–	–	–	–	–
LBL18-62-1	2a	B (3)	Average	12	3.4	5.8	6,800	13,000	3,000	310	150	9.1	4.6	87	53	160	1,300	10
			S.D.	3.3	1.3	2.1	2,000	13,000	680	180	120	9.0	4.0	47	4.0	64	350	3.0
LBL16-17-1	2a	B (5)	Average	12	3.7	7.0	14,000	9,600	3,000	460	160	4.7	6.7	99	75	100	1,600	20
			S.D.	2.9	1.7	2.7	2,500	7,600	600	200	47	3.2	4.6	26	30	48	360	6.6
LBL18-31-2	2a	B (2)	Average	13	5.0	4.2	11,000	10,000	3,500	580	130	4.2	4.7	110	73	23	2,400	12
			S.D.	4.8	1.1	2.8	160	1,300	1,100	160	21	5.9	6.6	45	52	26	1,400	5.2
LBL16-10-1	2a	V (6)	Average	1.5	0.39	0.55	1,400	7,800	280	43	16	n.d.	n.d.	9.1	10	10	160	6.5
			S.D.	0.41	0.18	0.29	660	3,200	140	13	5.0	–	–	3.2	4.5	8.5	110	0.071
LBL16-17-1	2a	V (3)	Average	0.99	0.46	0.68	370	11,000	260	41	14	0.68	3.4	7.8	7.1	7.7	130	5.4
			S.D.	0.79	0.26	0.53	110	5,500	250	19	10	0.61	4.1	3.9	1.9	2.4	140	2.6
LBL18-31-1	2a	V (5)	Average	1.3	0.48	0.75	1,400	8,200	400	39	12	0.26	5.2	6.8	17	13	210	5.9
			S.D.	0.30	0.24	0.31	320	4,700	240	19	4.1	0.58	12	3.3	18	17	120	5.8
LBL18-72-2	2a	V (5)	Average	1.1	0.42	0.88	760	7,100	300	49	10	0.64	3.3	7.3	6.3	13	130	1.9
			S.D.	0.28	0.10	0.20	500	4,700	36	10	4.2	1.4	6.1	2.2	2.5	15	66	0.74
LBL16-17-2	2a	L (3)	Average	0.10	0.28	0.97	1,100	8,400	230	31	19	n.d.	0.73	6.2	10	9.3	170	4.3
			S.D.	0.18	0.12	0.29	160	5,400	57	10	11	–	1.3	1.6	6.7	3.2	81	3.2
Stage 3																		
LBL16-6-1	3a	B (5)	Average	7.8	5.6	6.9	14,000	3,500	3,700	620	120	6.8	5.0	120	73	96	1,700	34
			S.D.	2.3	2.9	1.2	4,800	2,200	2,300	360	62	4.7	3.0	77	38	52	750	20
LBL18-42-2	3a	B (4)	Average	11	3.9	7.2	11,000	2,700	2,600	440	88	5.6	5.9	80	68	120	1,300	21
			S.D.	1.5	0.94	1.5	2,500	650	510	100	20	3.9	2.9	27	10	35	350	11

Table 6. *(Cont.)*

Assemblages	Vein type	Inclusion type (*n*)		Na (wt %)	K (wt %)	Fe (wt %)	Mn (ppm)	Cu (ppm)	Zn (ppm)	Rb (ppm)	Sr (ppm)	Mo (ppm)	Ag (ppm)	Cs (ppm)	Ba (ppm)	W (ppm)	Pb (ppm)	Bi (ppm)
Stage 3 *(cont.)*																		
LBL18-42-1	3a	B (8)	Average	11	4.0	4.7	11,000	3,700	3,500	560	130	12	6.5	95	88	100	2,500	26
			S.D.	3.0	1.8	1.1	3,200	3,500	620	100	54	26	4.0	27	34	52	750	29
LBL16-29-5	3a	B (5)	Average	8.3	3.5	4.5	15,000	1,800	4,200	360	320	10	3.1	140	160	80	2,400	40
			S.D.	0.73	0.96	1.3	4,400	3,300	2,200	150	200	21	4.6	110	120	7.1	730	40
LBL16-32-3	3a	B (6)	Average	10	5.0	7.4	14,000	4,300	4,000	640	150	14	8.4	89	99	130	2,500	20
			S.D.	2.2	1.2	2.2	3,800	2,400	1,100	200	38	12	1.3	29	31	68	540	3.9
LBL16-32-4	3a	B (9)	Average	8.6	4.2	5.5	10,000	3,000	3,700	480	160	12	8.1	87	90	66	2,300	26
			S.D.	1.6	1.3	1.1	1,900	2,300	860	130	50	10	2.5	17	27	71	700	18
LBL18-42-4	3b	B (4)	Average	11	3.1	5.0	11,000	3,400	2,400	350	360	n.d.	n.d.	86	360	92	1,200	34
			S.D.	1.9	0.68	1.9	6,600	3,300	420	84	350	–	–	37	450	2.8	590	32
LBL16-29-1	3b	B (5)	Average	7.6	4.9	5.9	12,000	3,200	3,900	560	130	2.1	10	120	57	68	2,100	78
			S.D.	2.6	0.55	2.4	4,500	2,500	920	89	31	2.9	2.6	31	23	51	390	94
LBL16-29-2	3b	B (5)	Average	7.6	4.9	0.70	14,000	2,400	3,400	570	110	7.3	8.9	92	62	140	1,800	16
			S.D.	2.3	0.99	1.1	3,000	1,300	600	150	43	5.9	1.8	22	12	99	560	2.1
LBL18-109-2	3c	B (3)	Average	6.4	4.2	6.5	8,300	2,200	1,700	500	140	0.90	1.2	230	58	210	1,200	64
			S.D.	0.25	0.31	0.56	700	610	170	26	5.8	0.78	1.1	21	5.7	30	58	3.1
LBL18-102-1	3c	B (3)	Average	5.8	4.3	6.3	8,200	2,300	1,800	490	140	1.2	0.91	230	92	140	1,200	60
			S.D.	0.6	0.93	1.3	1,400	1,000	210	66	15	0.52	0.90	31	40	110	100	7.8
LBL16-6-4	3a	V (5)	Average	0.85	0.27	0.36	640	5,500	230	32	12	1.8	2.4	7.2	7.1	10	94	5.5
			S.D.	0.22	0.067	0.23	330	3,700	83	12	6.6	2.6	2.7	2.1	4.5	5.8	31	2.1
LBL16-29-4	3a	V (7)	Average	0.74	0.36	0.25	940	3,700	340	32	14	0.090	1.4	6.2	6.6	3.3	130	5.9
			S.D.	0.48	0.19	0.18	350	4,800	210	19	8.8	0.24	3.1	3.4	1.2	2.6	96	5.4
LBL18-30-1	3b	V (4)	Average	0.67	0.20	0.51	790	3,100	170	24	10	0.073	0.33	4.7	3.2	4.6	61	1.8
			S.D.	0.19	0.11	0.28	500	1,300	120	11	2.5	0.15	0.65	2.0	1.9	2.8	56	–
LBL18-30-2	3b	V (4)	Average	1.7	n.d.	n.d.	n.d.	1,700	n.d.	5.7	16	1.6	n.d.	n.d.	n.d.	n.d.	40	n.d.
			S.D.	0.58	–	–	–	2,200	–	–	7.1	3.2	–	–	–	–	21	–
LBL18-42-3	3b	V (4)	Average	0.70	0.31	0.55	890	5,700	230	31	14	n.d.	2.1	8.5	3.5	3.5	130	1.7
			S.D.	0.20	0.093	0.24	330	750	35	12	9.4	–	1.7	3.3	1.4	2.5	15	0.53
LBL18-102-3	3c	V (4)	Average	0.67	0.24	0.20	350	4,000	180	14	10	0.29	0.35	4.1	n.d.	3.7	59	5.7
			S.D.	0.32	0.19	0.13	92	3,000	130	3.8	7.8	0.33	0.70	1.7	–	3.4	22	2.8
LBL18-109-2	3c	V (3)	Average	0.75	0.34	0.41	340	4,400	210	29	13	n.d.	n.d.	11	n.d.	14	63	3.6
			S.D.	0.17	0.20	0.16	7.1	1,900	130	7.8	6.5	–	–	0.12	–	4.2	34	3.0
Stage 4																		
LBL18-86-2	4a-2	B (4)	Average	6.1	4.0	5.9	9,100	3,000	4,400	650	30	0.61	2.4	84	150	46	3,000	16
			S.D.	0.68	1.0	0.45	2,400	1,200	500	96	28	1.0	3.0	9.4	67	32	500	5.6
LBL18-94-1	4a-2	B (3)	Average	5.6	4.1	6.7	11,000	2,600	4,300	660	150	0.40	5.7	82	230	64	2,500	17
			S.D.	2.7	3.3	1.7	6,100	1,500	2,200	270	200	0.69	5.0	11	300	92	660	7.8
LBL18-92-2	4a-2	B (4)	Average	3.0	7.4	7.3	19,000	3,100	8,600	870	46	0.63	8.4	130	140	72	5,800	32
			S.D.	0.86	1.3	0.60	6,000	1,200	4,100	140	6.7	1.1	3.9	51	140	49	2,700	24
LBL16-25-2	4a-1	B (3)	Average	7.8	3.0	2.0	7,900	270	4,400	260	280	0.43	2.1	170	90	31	2,200	12
			S.D.	1.9	0.53	2.5	5,900	220	2,000	75	240	0.75	1.8	180	56	51	723	11
LBL16-25-4	4a-1	B (2)	Average	8.5	5.4	6.0	12,000	270	6,700	490	160	n.d.	6.2	82	99	4.1	2,600	55
			S.D.	1.5	5.7	0.28	1,400	110	1,000	57	28	–	0.42	12	16	–	280	19
LBL18-42-5	4a-1	B (2)	Average	8.8	4.3	3.1	12,000	120	4,900	550	250	n.d.	3.4	130	160	1.9	2,200	26
			S.D.	0.071	2.1	0.14	710	52	3,300	300	35	–	4.7	86	28	–	280	11
LBL18-42-6	4a-1	B (3)	Average	6.9	2.7	4.1	14,000	180	7,300	240	230	0.73	3.8	180	110	69	1,700	43
			S.D.	1.6	0.76	1.8	5,600	71	4,000	140	120	1.3	4.1	140	62	59	200	49
LBL18-92-4	4a-2	V (3)	Average	0.22	0.30	0.27	510	130	350	28	3.1	n.d.	n.d.	3.5	5.9	2.4	180	1.0
			S.D.	0.066	0.085	0.10	270	97	240	7.9	4.1	–	–	0.35	2.9	3.2	140	0.50
LBL18-94-3	4a-2	V (6)	Average	0.29	0.35	0.24	460	250	280	34	0.76	n.d.	0.15	3.4	9.5	2.4	120	0.86
			S.D.	0.093	0.014	0.14	440	280	320	19	0.45	–	0.23	2.7	5.5	3.0	170	0.59

Table 6. (*Cont.*)

Assemblages	Vein type	Inclusion type (*n*)		Na (wt %)	K (wt %)	Fe (wt %)	Mn (ppm)	Cu (ppm)	Zn (ppm)	Rb (ppm)	Sr (ppm)	Mo (ppm)	Ag (ppm)	Cs (ppm)	Ba (ppm)	W (ppm)	Pb (ppm)	Bi (ppm)
Stage 4 (*cont.*)																		
LBL16-25-1	4a-1	V (8)	Average	0.46	0.27	0.15	240	120	110	22	4.1	0.37	0.048	3.2	11	4.1	46	1.5
			S.D.	0.14	0.38	0.13	210	39	52	22	2.4	0.69	0.13	0.92	15	3.1	39	1.6
LBL18-86-4	4a-2	V (5)	Average	0.47	0.25	0.25	820	110	350	21	7.1	0.24	n.d.	3.2	7.3	1.2	130	0.61
			S.D.	0.15	0.14	0.078	440	120	480	11	4.7	0.37	–	1.3	9.5	0.91	93	0.21
LBL16-25-3	4a-1	V (3)	Average	0.61	0.13	0.13	280	110	110	14	4.8	n.d.	n.d.	2.5	2.6	3.6	32	2.1
			S.D.	0.30	0.12	0.021	230	47	100	3.5	5.3	–	–	1.7	1.3	–	36	–
LBL18-86-3	4a-2	L (4)	Average	0.29	0.19	0.21	260	720	140	24	1.1	0.060	0.83	1.7	7.2	1.9	56	0.81
			S.D.	0.085	0.082	0.091	130	650	130	18	0.74	0.12	1.3	0.92	1.3	1.4	64	0.27
LBL18-92-4	4a-2	L (5)	Average	0.36	.0.22	0.13	390	370	140	16	4.7	n.d.	n.d.	1.9	14	11	34	0.71
			S.D.	0.12	0.14	0.086	240	380	82	6.8	–	–	–	0.69	13	16	39	0.42
LBL18-92-3	4a-2	L (5)	Average	0.35	0.34	0.19	790	210	290	30	8.2	0.12	0.19	4.5	7.2	4.1	170	1.9
			S.D.	0.17	0.24	0.12	230	85	240	16	15	0.26	0.29	3.3	5.6	2.2	140	2.0
LBL16-44-1	4b	L (4)	Average	0.52	0.099	0.030	600	18	99	7.6	10	n.d.	n.d.	6.6	3.0	0.49	40	0.42
			S.D.	0.090	0.070	0.013	710	–	120	5.8	6.4	–	–	5.9	2.2	–	53	–
LBL16-44-2	4b	L (5)	Average	0.35	0.14	0.36	150	26	n.d.	17	5.2	n.d.	n.d.	3.1	14	1.2	9.0	n.d.
			S.D.	0.094	0.072	–	110	7.1	–	16	6.2	–	–	1.2	–	–	–	–
LBL16-44-3	4b	L (4)	Average	0.63	0.20	0.071	490	14	57	17	31	n.d.	n.d.	3.5	3.1	8.3	34	n.d.
			S.D.	0.00	0.036	0.041	340	6.3	–	7.1	27	–	–	0.35	0.14	–	34	–

Notes: Data are reported as assemblage averages with standard deviation of 1σ
– = not calculated, *n* = number of analyzed inclusions, n.d. = not detected, S.D. = standard deviation
Fluid inclusion type: B = brine inclusion, L = liquid-rich inclusion, V = vapor-rich inclusion

similar concentrations in type V (up to 20,000 ppm) and type B inclusions (up to 28,000 ppm; Table 6). Approximately 75% of the type V inclusions have Mo and Ag concentrations lower than the detection limits (Table 6; App. 2). Type V inclusions from stage 1 to stage 3 veins display similar trace element concentrations (Table 6). Unlike type B inclusions, all type V inclusions from stage 4 have Cu contents one to two orders of magnitude lower than those in type V inclusions from the first three vein stages (typically <300 ppm; Table 6). The compositions of type L inclusions are similar to those of type V inclusions from the same stages, apart from stage 4b veins, where type L inclusions are depleted in most elements, including Fe (typically below detection limits), Cu (typically <40 ppm), Pb (typically <100 ppm), and Zn (typically below detection limits; Table 6).

Discussion

Origin and pressure-temperature-salinity evolution of ore-forming fluids

The Luoboling granodiorite porphyry pluton is interpreted to be the source of the porphyry mineralization at Luoboling (Jiang et al., 2013; Zhong et al., 2014). It is not clear whether the biotite granodiorite porphyry dikes or the Zhongliao biotite granodiorite pluton also contributed mineralization. Variations in Cs contents in magmatic-hydrothermal fluid can potentially be used to recognize multiple fluid pulses that originated from magmas at different stages of crystallization (Audétat and Pettke, 2003; Klemm et al., 2007, 2008). The Cs/(Na + K) ratios and Cs concentrations of fluid inclusions from different mineralization stages have limited variability at Luoboling (Fig. 10c, d; Table 6), consistent with a single magmatic-hydrothermal source (e.g., Klemm et al., 2007, 2008). These data, combined with previous geochronological results (Liang et al., 2012; Huang et al., 2013, 2018; Yu et al., 2013; Li and Jiang, 2014; Zhong et al., 2014; Pan et al., 2019), confirm that the Luoboling granodiorite porphyry was the only source of ore-forming fluids.

Fluid inclusions at Luoboling are dominated by vapor and brine (Figs. 2, 7; Tables 2, 3). Phase separation assemblages are widespread, in even the deepest barren quartz veins and quartz phenocrysts (Fig. 7). No obvious ID inclusions representing initial single-phase fluids were found in deep drill holes. Although a few L inclusions were observed in every stage (Fig. 7; Table 2), they have salinities and element compositions similar to those of corresponding vapor inclusions (Fig. 8; Table 6), rather than an intermediate composition between vapor and brine. We conclude that Luoboling formed at subcritical low-pressure conditions. Shallow emplacement of magma resulted in the initial fluids directly exsolving as brine and vapor, below the two-phase surface (Fig. 11; Bodnar et al., 1985; Richards, 2011; Kouzmanov and Pokrovski, 2012). According to mass balance calculations and observed inclusion populations in quartz phenocrysts, the initial vapor/brine mass ratios are estimated to be ~7:1. Pressure estimates based on fluid inclusions suggest that the deposit mainly formed at ~120 to 800 bar (Fig. 11), corresponding to mineralization depths of ~1.2 to 3.2 km, assuming that the veins in stage 1 formed under lithostatic pressure conditions and the veins in stage 4 formed under hydrostatic pressure conditions,

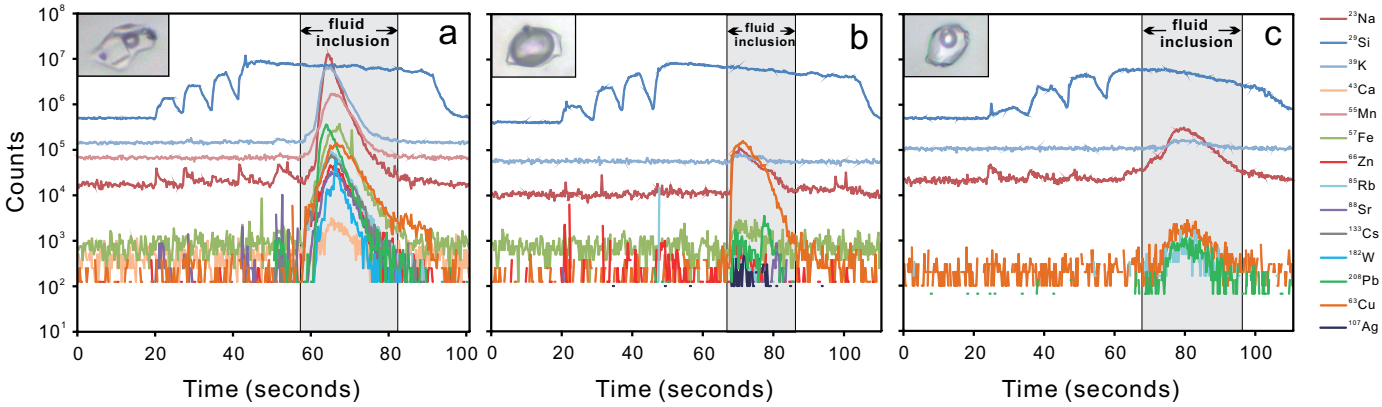

Fig. 9. Representative LA-ICP-MS signals of different fluid inclusion types at Luoboling. (a) Brine inclusion. (b) Vapor-rich inclusion. (c) Liquid-rich inclusion. The petrographic characteristics of corresponding fluid inclusions are pictured in the upper-left corner of each panel.

consistent with the results of Zhong et al. (2014). The earliest vapor-dominant fluids exsolved at ~500° to >600°C and ~500 to 800 bar, based on fluid inclusions in quartz phenocrysts and barren stage 1a veins. Later fluids recorded by type V and type B inclusions formed stage 2a veins at ~400° to 550°C and ~290 to 470 bar (Fig. 11) and stage 3a to stage 4a veins at ~250° to 450°C and ~120 to 360 bar. The increase in abundance of type B inclusions in stage 3 could relate to vapor loss due to a change to hydrostatic conditions. Because of the direct exsolution of brine and vapor, the fluids at Luoboling separated into two distinct end members: hypersaline type B inclusions that have salinities of 30 to 60 wt % NaCl equiv, and type V, L, and ID inclusions that have salinities typically lower than 10 wt % NaCl equiv (Figs. 8, 11a). Fluid salinities were consistent from stage 1 to stage 3 in both vapor and brine but decreased in different inclusion types at stage 4 (Figs. 8, 11a), implying the involvement of meteoric water in stage 4 fluids, consistent with H-O isotope results by Zhong et al. (2014).

Many type B inclusions were observed in stage 4a quartz-pyrite veins at Luoboling (Fig. 7o), indicate that hypersaline magmatic fluids were still present in the late stage of the hydrothermal system during quartz-muscovite alteration (Hedenquist et al., 1998; Harris and Golding, 2002; Rusk et al., 2004). There are distinct variations in type B inclusions from stage 4 relative to other stages in the log (K/Na)-log (Fe/Na) diagram (Fig. 10a), implying that brines were involved in the formation of associated phyllic alteration and suggesting a more significant effect of phyllic alteration relative to potassic alteration in modifying the fluid composition.

Minor type L inclusions occur in stage 1 to stage 3 veins, with homogenization temperatures mainly between 300° and 400°C and salinities and compositions similar to corresponding vapor inclusions (Fig. 8; Table 6). These inclusions are interpreted to be the products of vapor contraction, probably implying local aperture closure (Fig. 11; Heinrich et al., 2004). These aqueous liquids have similar densities (~0.6 g/cm^3), evolving along similar isochores after entrapment and intersecting with the two-phase surface between 300° and 400°C (Fig. 11). Type ID and L inclusions in stage 4a veins and type L inclusions in stage 4b veins with lower homogenization temperatures (189°–284°C) and higher densities (>0.8 g/cm^3) can be attributed to vapor contraction and/or different degrees of meteoric water involvement (Fig. 11).

Metal transport

The concentrations of Mo (up to 77 ppm) and other metals such as Fe, Pb, Zn, Cs, Ag, and W in type B inclusions at Luoboling are generally ~10 times higher than those in corresponding type V and L inclusions (Table 6; Fig. 12). Around 80% of type V and L inclusions have Mo contents below detection limits, indicating that the hypersaline liquid was the dominant phase transporting Mo (e.g., Ulrich et al., 1999; Audétat and Pettke, 2003; Klemm et al., 2007), consistent with recent partitioning experiments (Zajacz et al., 2017) and geologic observations that molybdenite mainly precipitated in the lower part of the orebody.

The transport of Cu in porphyry system is controversial, with arguments for brine or vapor transport (e.g., Henley and McNabb, 1978; Heinrich et al., 1999, 2004; Heinrich, 2005; Williams-Jones and Heinrich, 2005). Recently, several studies have proven that Cu can diffuse through channels in the quartz crystal lattice, resulting in anthropogenic enrichment of Cu in natural vapor inclusions during heating experiments (Zajacz et al., 2009; Lerchbaumer and Audétat, 2012; Seo and Heinrich, 2013). At Luoboling, apart from stage 4, Cu concentrations are similar in type V, B, and L inclusions (Fig. 12; Table 6). Although it is difficult to estimate the contribution of Cu by diffusion, several observations imply a more significant role for brine in transporting Cu:

1. Stage 3a and 3b veins host the bulk of chalcopyrite and also have the most abundant brine inclusions (Table 2; Fig. 7l, m).
2. Type B inclusions in stage 3 display varying Cu/(Na + K) ratios; however, Cu/(Na + K) ratios in type V inclusions are uniformly high (Fig. 10b), indicating limited Cu precipitation from vapor or significant Cu diffusion in type V inclusions.
3. Our mass balance calculations indicate that the brine in stage 3 chalcopyrite-bearing veins carried ~1.5 to 2.3 times more mass of Cu than the vapor, assuming that no diffusion occurred. If $D_{Cu}^{vapor/brine}$ values of 0.11 to 0.15

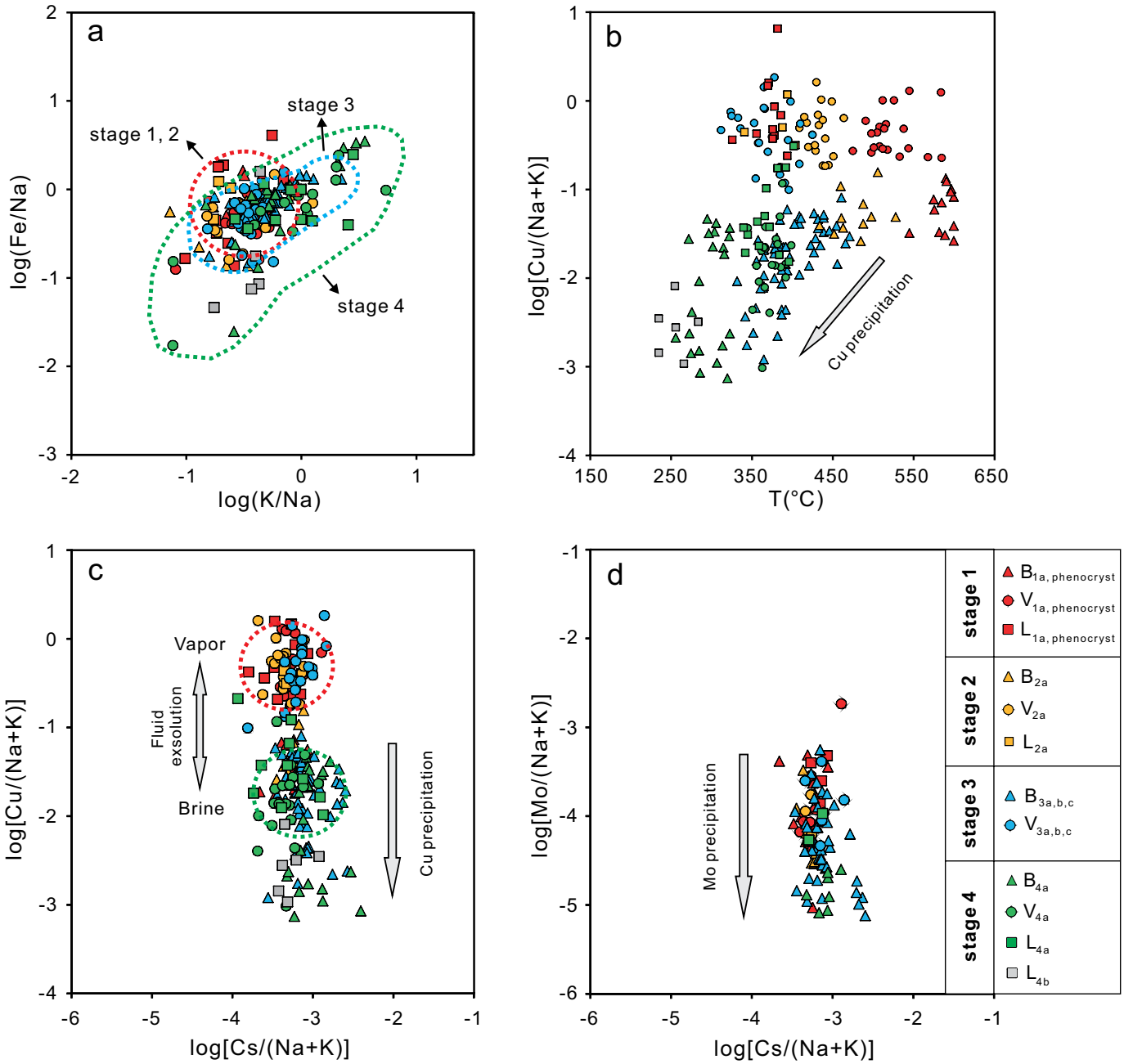

Fig. 10. Selected element ratio plots showing LA-ICP-MS data for individual fluid inclusions. (a) Fe/Na and K/Na ratios of inclusions have narrow ranges for stage 1 and stage 2 and exhibit positive correlations with each other for stage 3 and stage 4, indicating distinct modification of the fluids associated with phyllic alteration (stages 3 and 4) compared to potassic alteration (stages 1 and 2). (b) Cu/(Na + K) ratios are high in brine inclusions from stage 1 and stage 2 but decrease with decreasing temperatures in stage 3, interpreted to reflect the precipitation of Cu between 450° and 350°C. Cu/(Na + K) ratios of brine inclusions from stage 4 have two end members in stage 4a-1 and 4a-2 veins. Vapor-rich inclusions have high Cu/(Na + K) ratios from stage 1 to stage 3 but lower Cu/(Na + K) ratios in stage 4. Liquid-rich inclusions have Cu/(Na + K) ratios similar to corresponding vapor-rich inclusions. (c, d) Cs/(Na + K) ratios vary within a narrow range, indicating a single fluid source. Variations in Cu/(Na + K) and Mo/(Na + K) ratios are interpreted to be related to phase separation and precipitation of Cu and Mo.

were used (Lerchbaumer and Audétat, 2012), the brine would have carried ~12 to 27 times more Cu than vapor in stage 3 veins and ~1.1 to 1.5 times more masses of Cu than dominant vapor in stage 1.

4. Type B inclusions from stage 4 veins have an order of magnitude more Cu than type V inclusions (Fig. 12), implying the original distribution of Cu between brine and vapor.

Ore deposition

Molybdenite precipitation at Luoboling mainly occurred in the lower part of the deposit as abundant quartz-molybdenite

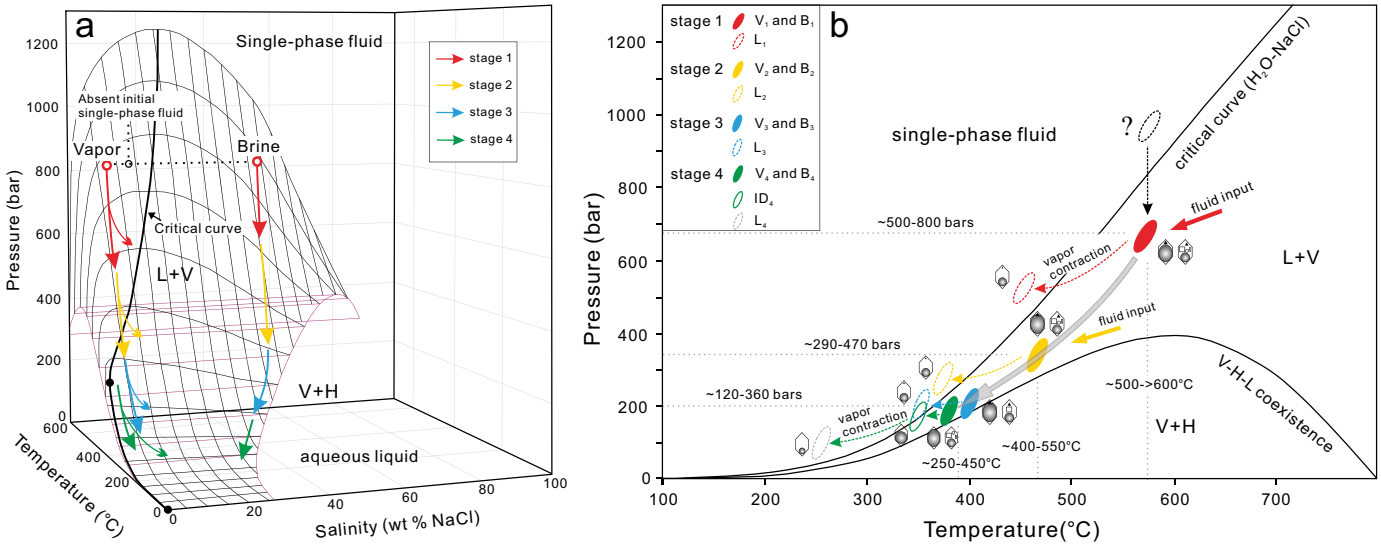

Fig. 11. Evolution of hydrothermal fluids at Luoboling in (a) temperature-pressure-salinity three-dimensional H_2O-NaCl phase diagram and (b) temperature-pressure two-dimensional phase diagram based on the H_2O-NaCl system after Driesner and Heinrich (2007). Shallow emplacement of the Luoboling pluton resulted in the absence of initial single-phase fluid and direct exsolution of vapor and brine from melt under the two-phase surface (e.g., Bodnar et al., 1985), with original vapor/brine mass ratios of ~7:1. Continuous cooling of fluids from ~600° to ~250°C and decompression from ~800 to ~120 bar are recorded by dominated type V and B inclusions from stage 1 to stage 4a veins. Type L inclusions from stage 1 to stage 3 have consistent homogenization temperatures mainly between 300° and 400°C and are interpreted to be the results of vapor contraction. Type L and ID inclusions from stage 4 are attributed to vapor contraction and/or involvement of meteoric water, as overall decrease of inclusion salinities in stage 4 veins.

veins (Figs. 2, 13). Decreases in Mo contents (Table 6) and significant variations in Mo/Na ratios for brine inclusions from stage 2 to stage 3 (Fig. 13) most likely reflect the processes of Mo precipitation. The shallow-level brine inclusions from stage 4 have Mo concentrations typically lower than 3 ppm, with most analyses below detection limits. The Mo/Na ratios of type B inclusions in stage 4 veins are up to two orders of magnitude lower relative to stage 1 (Fig. 13), implying the depletion of Mo in stage 4 fluids. K-feldspar-biotite alteration is the major alteration type associated with Mo mineralization and is also associated with barren stage 1 quartz veins (Fig. 5). Evidence of phase separation is preserved in the quartz phenocrysts and deep-seated barren quartz veins. Molybdenite-bearing stage 2 veins and barren stage 1 quartz veins have similar fluid inclusion assemblages, fluid compositions, alteration styles and H-O isotope characteristics (Zhong et al., 2014). The large temperature gap (more than 100°C) is the most obvious variable between these two vein stages (Fig. 8). The cooling of magmatic fluids to <500°C is therefore thought to be a key factor to trigger Mo precipitation at Luoboling. This temperature decrease may be related to the retraction of isotherms during the crystallization of magma, given the spatial superposition of stage 1 barren quartz veins and stage 2 molybdenite-bearing veins in the lower parts of the deposit (Figs. 2, 13) and their common crosscutting relationships (Fig. 5f).

Stage 3 Cu mineralization is located above the stage 2 Mo mineralization zone and is characterized by multiple substages of chalcopyrite-bearing veins (Table 2; Figs. 2, 13). Copper precipitation resulted in decreased Cu concentrations and Cu/Na ratios in type B inclusions from stage 3 veins (Table 6; Fig. 13). In Figure 10b, the variation of Cu/(Na + K) ratios in type B inclusions from stage 3 veins is up to two orders of magnitude, reflecting precipitation of chalcopyrite from high-salinity fluids. The end of Cu precipitation is recorded by the dramatic decreases in Cu/Na and Cu/(Na + K) ratios for vapor and liquid-rich inclusions in stage 4 veins and brine inclusions in stage 4a-1 veins (Figs. 10b, 13). A temperature decrease to 450° to 350°C appears to be related to chalcopyrite precipitation, similar to Mo precipitation at Luoboling, based on the decreasing trend of Cu/(Na + K) ratios with respect to homogenization temperatures of brine inclusions from 450° to 350°C in stage 3 (Fig. 10b). Fluid cooling triggering Cu precipitation, in contrast to Mo precipitation, was not only attributed to the retraction of isotherms but also related to the cooling during upward migration of early-stage fluids, which is suggested by the commonly shallower depths of Cu mineralization (Figs. 2, 13) and the transitional relationship between stage 2a, 3a, and 3b veins. It is likely that cooling reduced the solubility of Cu in stage 3 fluids (e.g., Crerar and Barnes., 1976; Hemley et al., 1992; Landtwing et al., 2005; Klemm et al., 2007). In addition, SO_2 progressively disproportionated to H_2S and H_2SO_4 when the fluid cooled, especially below ~400°C (Rye et al., 1992; Rye, 1993; Kusakabe et al., 2000; Reeves et al., 2010; Richards, 2011). This disproportionation is recorded by abundant hydrothermal anhydrite in stage 3 veins (Table 2). The generation of H_2S was significant for Cu precipitation as chalcopyrite from the brines (e.g., Rusk et al., 2004; Kouzmanov and Pokrovski, 2012), consistent with coexistence of chalcopyrite and anhydrite in stage 3 veins (Fig. 5l). The large amount of H^+ created by SO_2 disproportionation and chalcopyrite precipitation caused the pH of fluids to decrease, consistent with the evolution trend of alteration

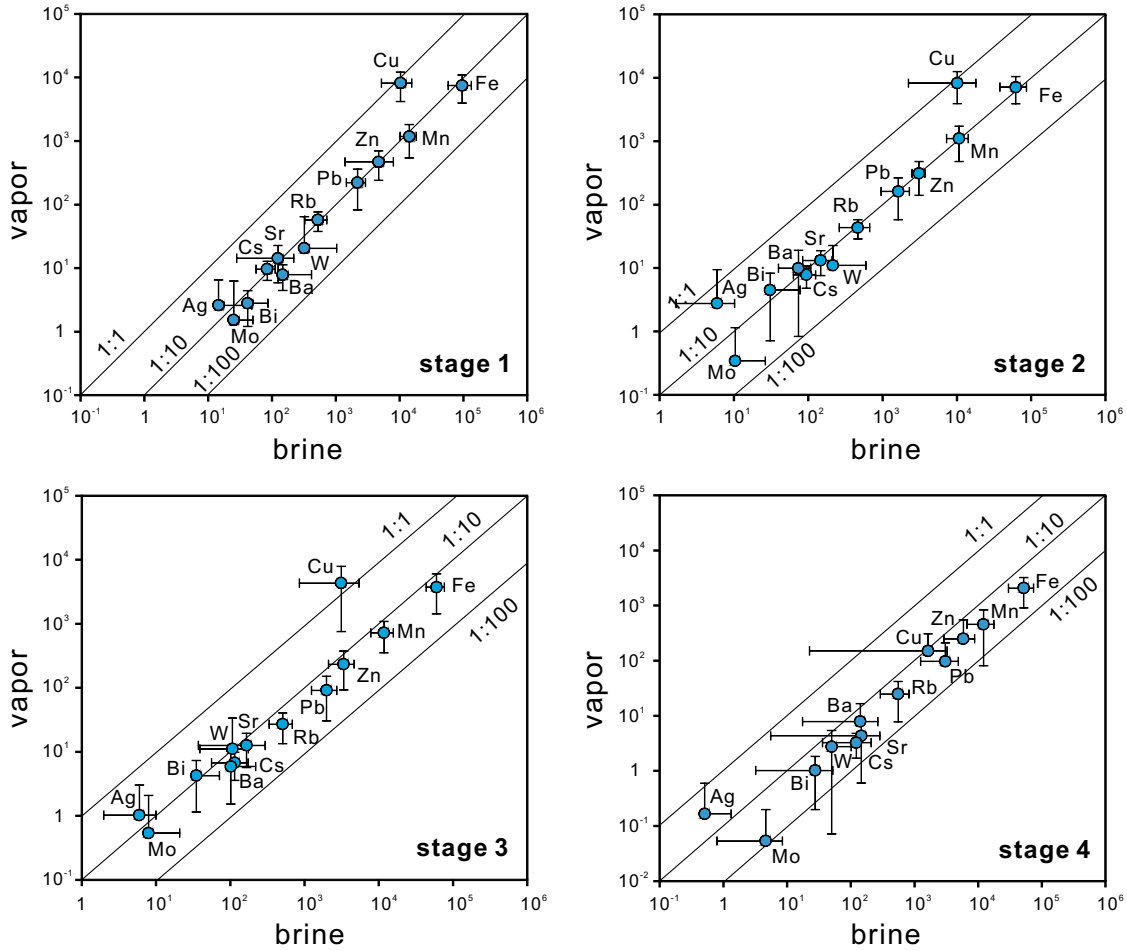

Fig. 12. Average element concentrations in brine versus concentrations in vapor inclusions from different mineralization stages. Note that the ratios of Cu contents in brine and vapor are nearly 1:1 in stage 1 to stage 3 but nearly 1:10 in stage 4. Error bars indicate 1σ variability. All data are presented in Table 6 and Appendix 2.

assemblages from K-feldspar-biotite, quartz-muscovite to kaolinite-muscovite-pyrite from stage 1 to stage 4 (Table 1).

The brine inclusions in shallow-level stage 4a-2 quartz-pyrite veins (Table 2; Figs. 2, 5n, 13) have high Cu/Na ratios and absolute Cu concentrations up to 4,700 ppm (Table 6; Fig. 13), although Cu-bearing sulfides are absent. These data indicate that stage 4a-2 veins formed from Cu-rich fluids that did not saturate with respect to Cu, possibly due to lower pH conditions of stage 4 fluids, consistent with the absence of chalcopyrite daughter minerals in brine inclusions (Fig. 7o) and intense phyllic alteration (Fig. 5n). It may be that these veins were feeders for shallow-level high-sulfidation Cu mineralization similar to that of Zijinshan, which has now been eroded. Type B inclusions in deep-seated stage 4a-1 quartz-pyrite veins have low Cu/Na ratios and Cu concentrations (typically <500 ppm; Table 2; Figs. 2, 5m, 13), indicating that these veins formed from Cu-poor fluids after Cu precipitation.

The L inclusions in stage 4b veins represent the last hydrothermal fluids at Luoboling. These inclusions have the lowest concentrations of most elements including Cu, Pb, and Zn (Table 6), marking the exhaustion of metals in the fluids and/or evident dilution effect of metal-poor meteoric water.

Implications for epithermal mineralization

A genetic relationship between the Luoboling porphyry Cu-Mo deposit and the adjacent Zijinshan high-sulfidation epithermal Cu-Au deposit has been the subject of considerable debate (e.g., Zhang et al., 2003; Zhong et al., 2014; Jiang et al., 2017; Li and Jiang, 2017; Huang et al., 2018; Chen et al., 2019; Pan et al., 2019). Pressure estimates indicate that Cu and Mo mineralization at Luoboling formed at ~1.2 to 1.9 km, similar to the estimated depth of Zijinshan (~1.4–2.1 km; Zhong et al., 2018), suggesting that Luoboling is not the deep part of Zijinshan and the present spatial relationship of these two deposits is not caused by a thrust fault. Our results are consistent with structural analyses by Chen et al. (2019), who argued that Luoboling and Zijisnhan are not related. Recently, a molybdenite weighted mean Re-Os age of 111.31 ± 0.70 Ma was obtained at Zijinshan (Zhao et al., 2020), consistent with newly reported muscovite ^{40}Ar-^{39}Ar (110.4 ± 1.3, 113.4 ± 1.1 Ma) and zircon U-Pb ages by Huang et al. (2018) from volcanic breccia (112.9 ± 1.2 Ma) and by Jiang et al. (2013) from dacite, dacite porphyry, and tuff (111 ± 0.3–110 ± 1 Ma). Direct comparison of molybdenite Re-Os ages eliminated errors caused by different dating methods

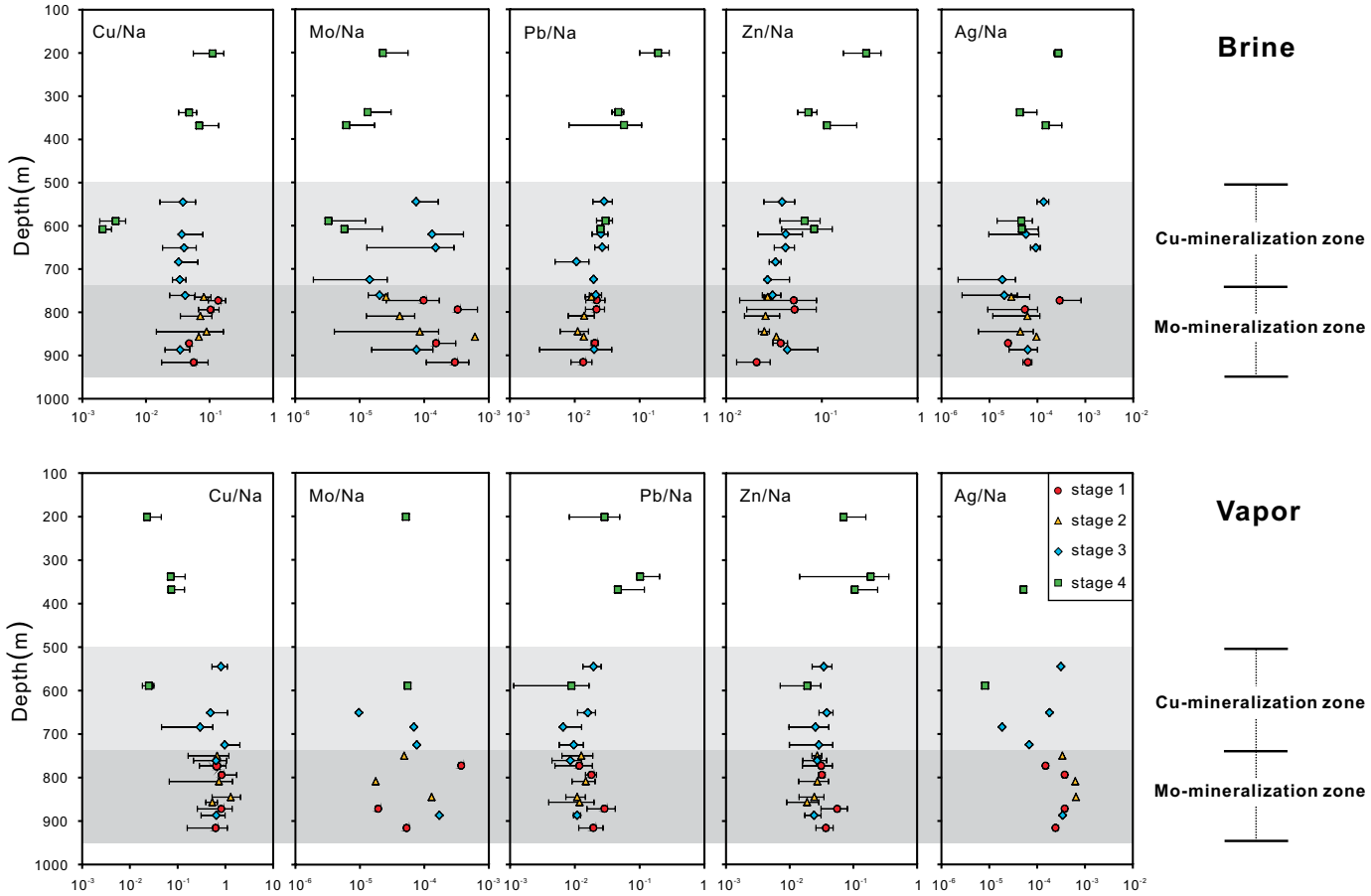

Fig. 13. Average ore-forming element concentration ratios relative to Na (metal/Na) in fluid inclusions from different mineralization stages and depths. The absolute depths of samples from different drill holes are transformed into relative depths based on drill hole ZK36-272. Error bars indicate 1σ variability. All data are presented in Table 6 and Appendix 2.

and indicates that the mineralization at Zijinshan most likely occurred earlier than Luoboling (with concentrated molybdenite Re-Os ages between 105.5 ± 2.2 and 104.6 ± 1.0 Ma; Liang et al., 2012; Zhong et al., 2014; Duan et al., 2017), consistent with the conclusions by Li and Jiang (2017) and Huang et al. (2018). In combination with our new data and previous studies (Li and Jiang, 2017; Huang et al., 2018; Chen et al., 2019), Zijinshan and Luoboling are concluded to be independent hydrothermal systems.

Brine inclusions from all stages at Luoboling host abundant Pb, Zn, and Ag. However, only limited galena has been observed in stage 3 veins. From stage 1 to stage 4, the Pb/Na and Zn/Na ratios increase obviously and Ag/Na ratios increase slightly in both vapor and brine inclusions (Fig. 13), implying that the effective precipitation of Pb, Zn, and Ag did not occur. Pb and Zn may continually migrate up and outward with fluids and precipitate in distal silicates (epidote for Pb, chlorite for Zn) to form the classic Pb-Zn halo around a porphyry orebody (Cooke et al., 2014, 2020; Wilkinson et al., 2015, 2020). Cooling of hypersaline liquid and involvement of meteoric water may cause effective precipitation of Pb, Zn, and Ag (Hemley and Hunt, 1992), eventually forming subepithermal Pb-Zn-Ag veins or epithermal Ag-Pb-Zn mineralization (Sillitoe, 2010), with the Yueyang deposit (southwest of Zijinshan) representing an example of this style of mineralization in the district. The presence of Paleozoic carbonates is permissive of skarn and/or distal carbonate replacement-style mineralization in the southeastern part of the district (Fig. 1c; Seward and Barnes, 1997; Sillitoe, 2010), although such mineralization is yet to be found.

Conclusions

Consistent Cs/(Na + K) ratios in fluid inclusions indicate that multistage ore-forming fluids at Luoboling were sourced from the Luoboling granodiorite. Shallow emplacement of magma caused direct exsolution of brines and vapors from melt below the two-phase surface. Based on microthermometry of fluid inclusions, the deposit mainly formed at 120 to ~800 bar (1.2–~3.2 km), with fluid temperatures mainly between 250° and 600°C and separated fluid salinities of 30 to 60 wt % NaCl equiv and <10 wt % NaCl equiv. The brines transported the bulk of both Mo and Cu, with Cu in vapor-rich inclusions likely related to Cu diffusion through quartz. The fluid temperature decreased to ~500°C and ~350° to 450°C and caused successive precipitation of Mo and Cu, respectively. The common late-stage quartz-pyrite veins in porphyry deposits can be formed from Cu-rich magmatic hydrothermal fluids. Luoboling is unrelated to the adjacent Zijinshan high-sulfidation epithermal Cu-Au deposit. Further exploration is thus suggested for another porphyry-style orebody underneath Zijinshan.

Acknowledgments

This research was financially supported by the National Key R&D Program of China (2016YFC0600405) and the National Natural Science Foundation of China (grant 41425011). The field work is strongly supported by the Zijin Mining Co. Ltd. We are grateful to Prof. David Cooke and an anonymous reviewer for their critical and constructive comments, which have greatly improved the quality of this paper. We especially thank Prof. David Cooke for his extremely detailed language polishing on our original manuscript. We also thank Shao-Hua Dong for help during SEM-CL imaging, Jia-Li Cai for help during fluid inclusion microthermometric analyses, and Yan-Wen Tang for help during LA-ICP-MS analyses of fluid inclusions.

REFERENCES

Audétat, A., and Pettke, T., 2003, The magmatic-hydrothermal evolution of two barren granites: A melt and fluid inclusion study of the Rito del Medio and Canada Pinabete plutons in northern New Mexico (USA): Geochimica et Cosmochimica Acta, v. 67, p. 97–121.

Bodnar, R.J., 1993, Revised equation and table for determining the freezing point depression of H_2O-NaCl solutions: Geochimica et Cosmochimica Acta, v. 57, p. 683–684.

Bodnar, R.J., Burnham, C.W., and Sterner, S.M., 1985, Synthetic fluid inclusions in natural quartz. III. Determination of phase equilibrium properties in the system H_2O-NaCl to 1000°C and 1500 bars: Geochimica et Cosmochimica Acta, v. 49, p. 1861–1873.

Chen, H.S., 1996, The research on the mineralization chronology and isotopic exploration assessment for Zijinshan copper-gold deposit: Geotectonica et Metallogenia, v. 20, p. 384–360 (in Chinese with English abs.).

Chen, J., Chen, Y.J., Zhong, J., Sun, Y., Li, J., and Qi, J.P., 2011, Fluid inclusion study of the Wuziqilong Cu deposit in the Zijinshan ore field, Fujian Province: Acta Petrologica Sinica, v. 27, p. 1425–1438 (in Chinese with English abs.).

Chen, J., Chen, Y.J., Zhong, J., Sun, Y., Qi, J.P., and Li, J., 2015, Geological and ore-fluid characteristics of Longjiangting Cu deposit in Zijinshan orefield, Fujian Province, and their genetic implications: Mineral Deposits, v. 34, p. 98–118 (in Chinese with English abs.).

Chen, J., Cooke, D.R., Piquer, J., Selley, D., Zhang, L., and White, N.C., 2019, Hydrothermal alteration, mineralization, and structural geology of the Zijinshan high-sulfidation Au-Cu deposit, Fujian Province, Southeast China: Economic Geology, v. 114, p. 639–666.

Cooke, D.R., Baker, M., Hollings, P., Sweet, G., Chang, Z.S., Danyushevsky, L., Gilbert, S., Zhou, T.F., White, N.C., Gemmell, J.B., and Inglis, S., 2014, New advances in detecting the distal geochemical footprints of porphyry systems—epidote mineral chemistry as a tool for vectoring and fertility assessments: Society of Economic Geologists, Special Publication 18, p. 127–152.

Cooke, D.R., Wilkinson, J.J., Baker, M., Agnew, P., Phillips, J., Chang, Z.S., Chen, H.Y., Wilkinson, C.C., Inglis, S., Hollings, P., Zhang, L.J., Gemmell, J.B., White, N.C., Danyushevsky, L., and Martin, H., 2020, Using mineral chemistry to aid exploration: A case study from the Resolution porphyry Cu-Mo deposit, Arizona: Economic Geology, v. 115, p. 813–840.

Crerar, D.A., and Barnes, H.L., 1976, Ore solution chemistry; V, Solubilities of chalcopyrite and chalcocite assemblages in hydrothermal solution at 200° to 350°C: Economic Geology, v. 71, p. 772–794.

Driesner, T., and Heinrich, C.A., 2007, The system H_2O-NaCl. Part I. Correlation formulae for phase relations in temperature-pressure-composition space from 0 to 1000°C, 0 to 5000 bar, and 0 to 1 XNaCl: Geochimica et Cosmochimica Acta, v. 71, p. 4880–4901.

Duan, G., Chen, H., Hollings, P., Qi, J., Xu, C., Zhang, S., Xiao, B., Liu, G.Y., and Liu, J., 2017, The Mesozoic magmatic sources and tectonic setting of the Zijinshan mineral field, South China: Constraints from geochronology and geochemistry of igneous rocks in the Southeastern ore segment: Ore Geology Reviews, v. 80, p. 800–827.

Goldstein, R.H., and Reynolds, T.J., 1994, Systematics of fluid inclusions in diagenetic minerals: Society of Sedimentary Geology (SEPM), Short Course 31, 199 p.

Guillong, M., Meier, D.L., Allan, M.M., Heinrich, C.A., and Yardley, B.W., 2008, SILLS: A MATLAB-based program for the reduction of laser ablation ICP-MS data of homogeneous materials and inclusions: Mineralogical Association of Canada Short Course Series, v. 40, p. 328–333.

Harris, A.C., and Golding, S.D., 2002, New evidence of magmatic-fluid related phyllic alteration: Implications for the genesis of porphyry copper deposits: Geology, v. 30, p. 335–338.

Hedenquist, J.W., Arribas, A., and Reynolds, T.J., 1998, Evolution of an intrusion-centered hydrothermal system; Far Southeast-Lepanto porphyry and epithermal Cu-Au deposits, Philippines: Economic Geology, v. 93, p. 373–404.

Heinrich, C.A., 2005, The physical and chemical evolution of low-salinity magmatic fluids at the porphyry to epithermal transition: A thermodynamic study: Mineralium Deposita, v. 39, p. 864–889.

Heinrich, C.A., Günther, D., Audétat, A., Ulrich, T., and Frischknecht, R., 1999, Metal fractionation between magmatic brine and vapor, determined by microanalysis of fluid inclusions: Geology, v. 27, p. 755–758.

Heinrich, C.A., Pettke, T., Halter, W.E., Aigner-Torres, M., Audetat, A., Gunther, D., Hanttendorf, B., Bleiner, D., Guillong, M., and Horn, I., 2003, Quantitative multi-element analysis of minerals, fluid, and melt inclusions by laser ablation-inductively coupled plasma-mass spectrometry: Geochimica et Cosmochimica Acta, v. 67, p. 3473–3496.

Heinrich, C.A., Driesner, T., Stefánsson, A., and Seward, T.M., 2004, Magmatic vapor contraction and the transport of gold from the porphyry environment to epithermal ore deposits: Geology, v. 32, p. 761–764.

Hemley, J.J., and Hunt, J.P., 1992, Hydrothermal ore-forming processes in the light of studies in rock-buffered systems; II. Some general geologic applications: Economic Geology, v. 87, p. 23–43.

Hemley, J.J., Cygan, G.L., Fein, J.B., Robinson, G.R., and d'Angelo, W.M., 1992, Hydrothermal ore-forming processes in the light of studies in rock-buffered systems; I. Iron-copper-zinc-lead sulfide solubility relations: Economic Geology, v. 87, p. 1–22.

Henley, R.W., and McNabb, A., 1978, Magmatic vapor plumes and groundwater interaction in porphyry copper emplacement: Economic Geology, v. 73, p. 1–20.

Hu, C.J., Huang, W.T., Bao, Z.W., Liang, H.Y., and Wang, C.L., 2012, LA-ICP-MS zircon U-Pb dating of the dacite porphyry from Zijinshan Cu-Au deposit and its metallogenic implications: Geotectonica et Metallogenia, v. 36, p. 284–292 (in Chinese with English abs.).

Huang, W.T., Li, J., Liang, H.Y., Wang, C.L., Lin, S.P., and Wang, X.Z., 2013, Zircon LA-ICP-MS U-Pb ages and highly oxidized features of magma associated with Luoboling porphyry Cu-Mo deposit in Zijinshan ore field, Fujian Province: Acta Petrologica Sinica, v. 29, p. 283–293 (in Chinese with English abs.).

Huang, W.T., Liang, H.Y., Wu, L., Wu, J., Li, J., and Bao, Z.W., 2018, Asynchronous formation of the adjacent epithermal Au-Cu and porphyry Cu-Mo deposits in the Zijinshan orefield, southeast China: Ore Geology Reviews, v. 102, p. 351–367.

Jiang, S.H., Liang, Q.L., Bagas, L., Wang, S.H., Nie, F.J., and Liu, Y.F., 2013, Geodynamic setting of the Zijinshan porphyry-epithermal Cu-Au-Mo-Ag ore system, SW Fujian Province, China: Constraints from the geochronology and geochemistry of the igneous rocks: Ore Geology Reviews, v. 53, p. 287–305.

Jiang, S.H., Bagas, L., and Liang, Q.L., 2017, Pyrite Re-Os isotope systematics at the Zijinshan deposit of SW Fujian, China: Constraints on the timing and source of Cu-Au mineralization: Ore Geology Reviews, v. 80, p. 612–622.

Klemm, L.M., Pettke, T., Heinrich, C.A., and Campos, E., 2007, Hydrothermal evolution of the El Teniente deposit, Chile: Porphyry Cu-Mo ore deposition from low-salinity magmatic fluids: Economic Geology, v. 102, p. 1021–1045.

Klemm, L.M., Pettke, T., and Heinrich, C.A., 2008, Fluid and source magma evolution of the Questa porphyry Mo deposit, New Mexico, USA: Mineralium Deposita, v. 43, p. 533–552.

Kouzmanov, K., and Pokrovski, G.S., 2012, Hydrothermal controls on metal distribution in porphyry Cu (-Mo-Au) systems: Society of Economic Geologists, Special Publication 16, p. 573–618.

Kusakabe, M., Komoda, Y., Takano, B., and Abiko, T., 2000, Sulfur isotopic effects in the disproportionation reaction of sulfur dioxide in hydrothermal fluids: Implications for the $\delta^{34}S$ variations of dissolved bisulfate and elemental sulfur from active crater lakes: Journal of Volcanology and Geothermal Research, v. 97, p. 287–307.

Lan, T.G., Hu, R.Z., Fan, H.R., Bi, X.W., Tang, Y.W., Zhou, L., Mao, W., and Chen, Y.H., 2017, In-situ analysis of major and trace elements in fluid inclusion and quartz: LA-ICP-MS method and applications to ore deposits: Acta Petrologica Sinica. v. 33, p. 3239–3262 (in Chinese with English abs.).

Lan, T.G., Hu, R.Z., Bi, X.W., Mao, G.J., Wen, B.J., Liu, L., and Chen, Y.H., 2018, Metasomatized asthenospheric mantle contributing to the generation of Cu-Mo deposits within an intracontinental setting: A case study of the ~128 Ma Wangjiazhuang Cu-Mo deposit, eastern North China craton: Journal of Asian Earth Sciences, v. 160, p. 460–489.

Landtwing, M.R., Pettke, T., Halter, W.E., Heinrich, C.A., Redmond, P.B., Einaudi, M.T., and Kunze, K., 2005, Copper deposition during quartz dissolution by cooling magmatic-hydrothermal fluids: The Bingham porphyry: Earth and Planetary Science Letters, v. 235, p. 229–243.

Lerchbaumer, L., and Audétat, A., 2012, High Cu concentrations in vapor-type fluid inclusions: An artifact?: Geochimica et Cosmochimica Acta, v. 88, p. 255–274.

Li, B., and Jiang, S.Y., 2015, A subduction-related metasomatically enriched mantle origin for the Luoboling and Zhongliao Cretaceous granitoids from the Zijinshan ore district of Fujian Province in South China: Implications for magma evolution and Cu-Mo mineralization: International Geology Review, v. 57, p. 1239–1266.

——2017, Genesis of the giant Zijinshan epithermal Cu-Au and Luoboling porphyry Cu-Mo deposits in the Zijinshan ore district, Fujian Province, SE China: A multi-isotope and trace element investigation: Ore Geology Reviews, v. 88, p. 753–767.

Li, B., Zhao, K.D., Yang, S.Y., and Dai, B.Z., 2013, Petrogenesis of the porphyritic dacite from Ermiaogou Cu-Au deposit in Zijinshan ore field and its metallogenetic implications: Acta Petrologica Sinica. v. 29, p. 4167–4185 (in Chinese with English abs.).

Li, B., Jiang, S.Y., Lu, A.H., Zhao, H.X., Yang, T.L., and Hou, M.L., 2016, Zircon U-Pb dating, geochemical and Sr-Nd-Hf isotopic characteristics of the Jintonghu monzonitic rocks in western Fujian Province, South China: Implication for Cretaceous crust-mantle interactions and lithospheric extension: Lithos, v. 260, p. 413–428.

Liang, Q.L., Jiang, S.H., Wang, S.H., Li, C., and Zeng, F.G., 2012, Re-Os dating of molybdenite from the Luoboling porphyry Cu-Mo deposit in the Zijinshan ore field of Fujian province and its geological significance: Acta Geologica Sinica, v. 86, p. 1113–1118 (in Chinese with English abs.).

Liu, W.Y., Cook, N.J., Ciobanu, C.L., Liu, Y., Qiu, X.P., and Chen, Y.C., 2016, Mineralogy of tin-sulfides in the Zijinshan porphyry-epithermal system, Fujian Province, China: Ore Geology Reviews, v. 72, p. 682–698.

Liu, W.Y., Chen, Y.C., and Liu, Y., 2017, EPMA and LA-ICP-MS microanalysis of Cu-Fe-S minerals in Zijinshan orefield: Implications for ore genesis: Earth Science Frontiers, v. 24, p. 39–53 (in Chinese with English abs.).

Mao, J.W., Li, X.F., White, N.C., Zhao, C.S., Zhang, Z.H., Wang, Y.T., and Hu, H.B., 2007, Types, characteristics, and geodynamic settings of Mesozoic epithermal gold deposits in eastern China: Resource Geology, v. 57, p. 435–454.

Mao, J.W., Cheng, Y.B., Chen, M.H., and Pirajno, F., 2013, Major types and time-space distribution of Mesozoic ore deposits in South China and their geodynamic settings: Mineralium Deposita, v. 48, p. 267–294.

Pan, J.Y., Ni, P., Chi, Z., Wang, W.B., Zeng, W.C., and Xue, K., 2019, Alunite $^{40}Ar/^{39}Ar$ and zircon U-Pb constraints on the magmatic-hydrothermal history of the Zijinshan high-sulfidation epithermal Cu-Au deposit and the adjacent Luoboling porphyry Cu-Mo deposit, South China: Implications for their genetic association: Economic Geology, v. 114, p. 667–695.

Piquer, J., Cooke, D.R., Chen, J., and Zhang, L., 2017, Synextensional emplacement of porphyry Cu-Mo and epithermal mineralization: The Zijinshan district, southeastern China: Economic Geology, v. 112, p. 1055–1074.

Qiu, X.P., Lan, Y.Z., and Liu, Y., 2010, The key to the study of deep mineralization and the evaluation of ore-prospecting potential in the Zijinshan gold and copper deposit: Acta Geoscientica Sinica, v. 31, p. 209–215 (in Chinese with English abs.).

Reeves, E.P., Seewald, J.S., Saccocia, P., Walsh, E., Bach, W., Craddock, P.R., Shanks, W.C., Sylva, S.P., Pichler, T., and Rosner, M., 2010, Geochemistry of hydrothermal fluids from the PACMANUS, Northeast Pual and Vienna Woods hydrothermal fields, Manus basin, Papua New Guinea: Geochimica et Cosmochimica Acta, v. 75, p. 1088–1123.

Richards, J.P., 2011, Magmatic to hydrothermal metal fluxes in convergent and collided margins: Ore Geology Reviews, v. 40, p. 1–26.

Rusk, B.G., Reed, M.H., Dilles, J.H., Klemm, L.M., and Heinrich, C.A., 2004, Compositions of magmatic hydrothermal fluids determined by LA-ICP-MS of fluid inclusions from the porphyry copper-molybdenum deposit at Butte, MT: Chemical Geology, v. 210, p. 173–199.

Rye, R.O., 1993, The evolution of magmatic fluids in the epithermal environment: The stable isotope perspective: Economic Geology, v. 88, p. 733–753.

Rye, R.O., Bethke, P.M., and Wassrman, M.D., 1992, The stable isotope geochemistry of acid sulfate alteration: Economic Geology, v. 87, p. 225–262.

Seo, J.H., and Heinrich, C.A., 2013, Selective copper diffusion into quartz-hosted vapor inclusions: Evidence from other host minerals, driving forces, and consequences for Cu-Au ore formation: Geochimica et Cosmochimica Acta, v. 113, p. 60–69.

Seward, T.M., and Barnes, H.L., 1997, Metal transport by hydrothermal ore fluids, *in* Barnes, H.L., ed., Geochemistry of hydrothermal ore deposits, 3rd ed.: New York, Wiley, p. 435–486.

Sillitoe, R.H., 2010, Porphyry copper systems: Economic Geology, v. 105, p. 3–41.

So, C.S., Zhang, D.Q., Yun, S.T., and Li, D.X., 1998, Alteration-mineralization zoning and fluid inclusions of the high sulfidation epithermal Cu-Au mineralization at Zijinshan, Fujian Province, China: Economic Geology, v. 93, p. 961–980.

Steele-MacInnis, M., Lecumberri-Sanchez, P., and Bodnar, R.J., 2012, Short note: HokieFlincs_ H2O-NaCl: A Microsoft Excel spreadsheet for interpreting microthermometric data from fluid inclusions based on the PVTX properties of H_2O-NaCl: Computers and Geosciences, v. 49, p. 334–337.

Sterner, S.M., Hall, D.L., and Bodnar, R.J., 1988, Synthetic fluid inclusions. V. Solubility relations in the system NaCl-KCl-H_2O under vapor-saturated conditions: Geochimica et Cosmochimica Acta, v. 52, p. 989–1005.

Ulrich, T., Guenther, D., and Heinrich, C.A., 1999, Gold concentrations of magmatic brines and the metal budget of porphyry copper deposits: Nature, v. 399, p. 676–679.

Wang, S.H., Pei, R.F., Zeng, X.H., Qiu, X.P., and Wei, M., 2009, Metallogenic series and model of the Zijinshan mining field: Acta Geologica Sinica, v. 83, p. 145–157 (in Chinese with English abs.).

Wilkinson, J.J., Chang Z.S., Cooke, D.R., Baker, M.J., Wilkinson, C.C., Inglis, S., Chen, H.Y., and Gemmell, J.B., 2015, The chlorite proximitor: A new tool for detecting porphyry ore deposits: Journal of Geochemical Exploration, v. 152, p. 10–26.

Wilkinson, J.J., Baker, M.J., Cooke, D.R., and Wilkinson, C.C., 2020, Exploration targeting in porphyry Cu systems using propylitic mineral chemistry: A case study of the El Teniente deposit, Chile: Economic Geology, v. 115, p. 771–791.

Williams-Jones, A.E., and Heinrich, C.A., 2005, 100th Anniversary special paper: Vapor transport of metals and the formation of magmatic-hydrothermal ore deposits: Economic Geology, v. 100, p. 1287–1312.

Wu, L.Y., Hu, R.Z., Qi, Y.Q., and Zhu, J.J., 2013, Zircon LA-ICP-MS U-Pb ages and geochemical characteristics of quartz syenite porphyry from Jintonghu deposit in Zijinshan ore field, Fujian Province, South China: Acta Petrologica Sinica, v. 29, p. 4151–4166 (in Chinese with English abs.).

Wu, L.Y., Hu, R.Z., Li, X.F., Liu, S.A., Tang, Y.W., and Tang, Y.Y., 2017, Copper isotopic compositions of the Zijinshan high-sulfidation epithermal Cu-Au deposit, South China: Implications for deposit origin: Ore Geology Reviews, v. 83, p. 191–199.

Wu, L.Y., Hu, R.Z., Li, X.F., Stuart, F.M., Jiang, G.H., Qi, Y.Q., and Zhu, J.J., 2018, Mantle volatiles and heat contributions in high sulfidation epithermal deposit from the Zijinshan Cu-Au-Mo-Ag orefield, Fujian Province, China: Evidence from He and Ar isotopes: Chemical Geology, v. 480, p. 58–65.

Xu, C., Chen, H.Y., Huang, W.T., Qi, J.P., Duan, G., Zhang, L.J., Wu, C., Zhang, S., and Zhong, W.B., 2017, Mesozoic multiphase magmatism at the Xinan Cu-Mo ore deposit (Zijinshan orefield): Geodynamic setting and metallogenic implications: Ore Geology Reviews, v. 88, p. 768–790.

Xue, K., and Ruan, S.K., 2008, Geological characteristics and genesis of the Luoboling copper (molybdenum) deposit in Zijinshan orefield, Fujian: Resources Environment and Engineering, v. 22, p. 491–496 (in Chinese with English abs.).

Yu, B., Pei, R.F., Qiu, X.P., Chen, J.H., Li, D.P., Zhang, W.H., and Liu, W.Y., 2013, The evolution series of Mesozoic magmatic rocks in the Zijinshan orefield, Fujian Province: Acta Geologica Sinica, v. 34, p. 437–446 (in Chinese with English abs.).

Zajacz, Z., Hanley, J.J., Heinrich, C.A., Halter, W.E., and Guillong, M., 2009, Diffusive reequilibration of quartz-hosted silicate melt and fluid inclusions: Are all metal concentrations unmodified?: Geochimica et Cosmochimica Acta, v. 73, p. 3013–3027.

Zajacz, Z., Candela, P.A., and Piccoli, P.M., 2017, The partitioning of Cu, Au and Mo between liquid and vapor at magmatic temperatures and its implications for the genesis of magmatic-hydrothermal ore deposits: Geochimica et Cosmochimica Acta, v. 207, p. 81–101.

Zhang, D.Q., Li, D.X., Zhao, Y.M., Chen, J.H., Li, Z.L., and Zhang, K.Y., 1991, The Zijinshan deposit: The first example of quartz-alunite type

epithermal deposits in the continent of China: Geological Review, v. 37, p. 481–491 (in Chinese with English abs.).
Zhang, D.Q., Li, D.X., Feng, C.Y., and Dong, Y.J., 2001, The temporal and spatial framework of the Mesozoic magmatic system in Zijinshan area and its geological significance: Acta Geoscientia Sinica, v. 22, p. 403–408 (in Chinese with English abs.).
Zhang, D.Q., She, H.Q., Li, D.X., and Feng, C.Y., 2003, The porphyry-epithermal metallogenic system in the Zijinshan region, Fujian Province: Acta Geologica Sinica, v. 77, p. 254–261 (in Chinese with English abs.).
Zhang, D.Q., Feng, C.Y., Li, D.X., She, H.Q., and Dong, Y.J., 2005, The evolution of ore-forming fluids in the porphyry-epithermal metallogenic system of Zijinshan area: Acta Geoscientica Sinica, v. 26, p. 127–136 (in Chinese with English abs.).
Zhang, J.Z., 2013, Geology, exploration model and practice of Zijinshan ore concentrated area: Mineral Deposits, v. 32, p. 757–766 (in Chinese with English abs.).
Zhao, X.L., Mao, J.R., Chen, R., and Xu, N.Z., 2008, SHRIMP zircon dating of the Zijinshan pluton in southwestern Fujian and its implications: Geology in China, v. 35, p. 590–597 (in Chinese with English abs.).
Zhao, X.Y., Zhong, H., Mao, W., Bai, Z.J., and Xue, K., 2020, Molybdenite Re-Os dating and LA-ICP-MS trace element study of sulfide minerals from the Zijinshan high-sulfidation epithermal Cu-Au deposit, Fujian Province, China: Ore Geology Reviews, v. 118, article 103363.
Zhong, J., Chen, Y.J., Chen, J., Li, J., Qi, J.P., and Dai, M.C., 2011, Fluid inclusion study of the Luoboling porphyry Cu-Mo deposit in the Zijinshan ore field, Fujian Province: Acta Petrologica Sinica, v. 27, p. 1410–1424 (in Chinese with English abs.).
Zhong, J., Chen, Y.J., Pirajno, F., Chen, J., Li, J., Qi, J.P., and Li, N., 2014, Geology, geochronology, fluid inclusion and H-O isotope geochemistry of the Luoboling porphyry Cu-Mo deposit, Zijinshan orefield, Fujian Province, China: Ore Geology Reviews, v. 57, p. 61–77.
Zhong, J., Chen, Y.J., Qi, J.P., Chen, J., Dai, M.C., and Li, J., 2017, Geology, fluid inclusion and stable isotope study of the Yueyang Ag-Au-Cu deposit, Zijinshan orefield, Fujian Province, China: Ore Geology Reviews, v. 86, p. 254–270.
Zhong, J., Chen, Y.J., Chen, J., Qi, J.P., and Dai, M.C., 2018, Geology and fluid inclusion geochemistry of the Zijinshan high-sulfidation epithermal Cu-Au deposit, Fujian Province, SE China: Implication for deep exploration targeting: Journal of Geochemical Exploration, v. 184, p. 49–65.
Zhou, S., and Chen, H.S., 1996, Geochronology and geological significance of the Zijinshan copper-gold deposit: Petrology and Geochemistry, v. 15, p. 216–219 (in Chinese with English abs.).

Xiao-Yu Zhao received his bachelor's degree in geology from Northwest University in 2015. He was then recommended to Institute of Geochemistry, Chinese Academy of Sciences, to study, and he received his doctoral degree in geochemistry in 2020. He is now working at Kunming University of Science and Technology. His current research interest focuses on porphyry-epithermal mineralization systems, especially the evolution process of ore-forming fluids.